J. Fluid Mech. (2014), *vol.* 748, *pp.* 368–398. © Cambridge University Press 2014
doi:10.1017/jfm.2014.185

Perturbing vortex packets in a turbulent boundary layer

Shaokai Zheng and Ellen K. Longmire†

Department of Aerospace Engineering and Mechanics, University of Minnesota, Minneapolis, MN 55455, USA

(Received 11 September 2013; revised 21 January 2014; accepted 1 April 2014; first published online 29 April 2014)

A zero pressure gradient turbulent boundary layer of $Re_\tau = 2500$ was perturbed by a single spanwise array of finite cylinders mounted on the bounding surface and extending through the logarithmic region. The cylinder height was $H/\delta = 0.2$ ($H^+ = 500$), where δ is the boundary layer thickness, with an aspect ratio (AR) (height/diameter) of four. Streamwise–spanwise (x–y) planes of the flow were examined by particle image velocimetry (PIV) up to 7δ downstream at a wall-normal location of $z^+ = 300$ for cylinder array spacings ranging from 0.2δ to 0.8δ. Average streamwise velocity fields showed a splitting, then merging pattern of cylinder wakes which occurred further downstream as the cylinder spacing increased. Based on measurements at the furthest downstream location, both the spanwise variation of average streamwise velocity and the Fourier content in the instantaneous fields suggested that the case with 0.6δ cylinder spacing, which matched the dominant spanwise scale in the unperturbed flow, yielded the most persistent downstream flow organization. A flying PIV method was implemented to track specific packet structures over a range $-2 < x/\delta < 7$ with respect to the cylinder array, corresponding to a time scale of $12.4\delta/U_\infty$. Packets approaching the 0.2δ spacing array first lost their organization but then regained it a distance 2δ downstream, suggesting that a persistent outer layer organization propagated inwards into the log region. For arrays with larger spanwise spacing, approaching packets were generally redirected into the spanwise location midway between cylinders and sometimes enhanced.

Key words: boundary layer structure, turbulent boundary layers, turbulence control

1. Introduction

Many previous studies of wall-bounded turbulent flow have shown the existence of coherent groups of hairpin vortices in the logarithmic and outer regions that are roughly aligned in the streamwise direction, referred to as vortex packets (Zhou *et al.* 1999; Christensen & Adrian 2001; Adrian & Liu 2002; Ganapathisubramani, Longmire & Marusic 2003; Adrian 2007; Elsinga *et al.* 2007; Dennis & Nickels 2011*a*; Gao, Ortiz-Dueñas & Longmire 2013). Since these packet structures are believed to be important for the production and sustainment of turbulence, it may be possible to alter boundary layer behaviour by manipulating these packets. In the present study,

† Email address for correspondence: longmire@umn.edu

https://doi.org/10.1017/jfm.2014.185 Published online by Cambridge University Press

we seek to understand how a single array of obstructions embedded in the boundary layer can alter the vortex packet organization. We first discuss the features and scaling of vortex packets and then describe the effects of embedded perturbations based on the previous literature. In all the following discussions, x, y and z are defined as streamwise, spanwise and wall-normal directions respectively.

1.1. *Vortex packets*

The hairpins within packets are typically forward leaning (Adrian, Meinhart & Tomkins 2000; Ganapathisubramani, Longmire & Marusic 2006) so that they induce $Q2$ (ejection) events as well as negative streamwise velocity fluctuations ($u < 0$) creating long low-momentum regions (LMRs) in the streamwise direction (Tomkins & Adrian 2003). The features of these LMRs have been studied extensively over the past decade. Hutchins, Hambleton & Marusic (2005*a*), who compared the spanwise and wall-normal extent of u, v and w two-point correlations for data at $Re_\tau = 690$–2800, found that they all scaled with outer variables, which was consistent with the earlier findings of Wark, Naguib & Robinson (1991). Therefore, outer scaling will be used typically for further discussions in this paper. Relatively long streamwise-aligned packets have been found to predominate in the logarithmic region of the boundary layer (Ganapathisubramani *et al.* 2003; Elsinga *et al.* 2007; Lee & Sung 2011), but also extend into the outer region (Adrian 2007; Elsinga *et al.* 2010*a*). The outer packets have been demonstrated to make a significant imprint on the near-wall region, seeming to modulate smaller scale events at the wall (Hutchins & Marusic 2007; Mathis, Hutchins & Marusic 2009).

Hutchins & Marusic (2007), who considered data over the range $Re_\tau = 1 \times 10^3 - 6 \times 10^5$, reported length scales of LMRs of up to 20δ. The length scales were observed to grow as the Reynolds number increased. For experiments at $Re_\tau = 2460$, Dennis & Nickels (2011*b*) reported LMR length scales to be predominantly 2–3δ, with 97 % of all structures having lengths less than 7δ. They interpreted the concept of very-large-scale structures as resulting from the streamwise alignment of multiple shorter structures. This concept was supported by Lee & Sung (2011), whose direct numerical simulations (DNSs) yielded estimates of streamwise coherence to be of the order of 6δ in the log region.

Tomkins & Adrian (2003), who studied LMRs at different wall-normal heights in the logarithmic region ($z^+ = 100$–440) of a turbulent boundary layer at $Re_\tau = 2216$, found that the regions of low u-momentum, which extended 2δ or more in the streamwise direction, had spanwise widths of 0.1–0.4δ, which increased with distance from the wall. This implies that the distance between the hairpin legs also increases with wall-normal distance. As the size increases, spanwise interactions between hairpins become more likely. The authors proposed three possible vortex merging scenarios, based on their relative position at the time of encounter, as a mechanism for spanwise scale growth. Based on tracking measurements using tomographic particle image velocimetry (PIV) in a turbulent boundary layer at $Re_\tau = 2480$, Gao (2011) and Longmire *et al.* (2011) reported spanwise widths of the LMRs of 0.1–0.2δ at $z^+ = 200$ and 0.26–0.3δ at $z^+ = 400$, which was consistent with the results of Tomkins & Adrian (2003).

Although the scales of individual LMRs in the logarithmic and outer regions have been studied extensively, studies regarding the spacing between them are more limited. Hutchins, Ganapathisubramani & Marusic (2005*b*) studied the spanwise periodicity of the LMRs in DNS data at $Re_\tau = 1100$, by looking at the spanwise Fourier modes of

https://doi.org/10.1017/jfm.2014.185 Published online by Cambridge University Press

the streamwise velocity variations at $z^+ = 150$. They found the most probable spanwise spacing of the LMRs to be 0.6δ. Elsinga *et al.* (2010*a*) reported spanwise spacings between the LMRs to be 0.5–1δ in a supersonic turbulent boundary layer at $Re_\tau = 7080$, and Gao (2011) proposed the spanwise spacing of these structures to be larger than 0.5δ in the log region.

Some recent studies have also investigated the temporal development of individual hairpins and eddies in the boundary layer. Elsinga & Marusic (2010) probed time-resolved tomographic-PIV data by examining the invariants of the velocity gradient tensor; they proposed a characteristic lifetime for the energy-containing eddies in the outer region of the boundary layer as $14.3\delta/U_\infty$. Atkinson *et al.* (2012) obtained a value of $12.5\delta/U_\infty$ for a comparable wall-normal range extracted from DNS data. Elsinga *et al.* (2012) examined the streamwise-aligned, spanwise vortices using the same data and suggested that they interact on a time scale of the order of δ/U_∞. LeHew, Guala & McKeon (2013) used time-resolved PIV in streamwise–spanwise planes to track individual swirling structures and found that some persisted longer than $5\delta/U_\infty$. Gao (2011) applied a flying tomographic-PIV system to track the LMRs over a streamwise distance of 15.5δ (duration of $21.3\delta/U_\infty$) and observed spanwise meandering over distances of 0.12δ. Gao *et al.* (2013) further analyzed the same data set, and reported merging events that occurred over time scales of 3.2–$6.4\delta/U_\infty$. The present investigation will use planar PIV (PPIV) and stereoscopic PIV (SPIV) data to further the understanding of eddy and packet evolution over distances of 9δ (equivalent time scales up to $12.4\delta/U_\infty$).

1.2. *Perturbations to turbulent boundary layers*

In the present investigation, we seek to apply perturbations to boundary layers that are fully turbulent. To minimize obstruction, we consider a single, relatively sparse array of discrete obstacles with heights of 0.2δ that extend into the logarithmic region, but not beyond, so that the obstacle height is relatively small compared to the boundary layer thickness. Although a wealth of previous work on flow over canopies (Belcher, Jerram & Hunt 2003; Castro, Cheng & Reynolds 2006; Coceal *et al.* 2007) and rough-walled boundary layers (Tomkins 2001; Jiménez 2004; Orlandi, Leonardi & Antonia 2006; Ikeda & Durbin 2007; Wu & Christensen 2010; Guala *et al.* 2012) considers elements of relatively small height, the elements typically are distributed over a significant streamwise distance, and the resulting effects are substantially different from those investigated herein. Our discussion below is therefore limited to the effect of individual or single arrays of obstructions on downstream characteristics.

Many studies have shown that small obstacles inserted in turbulent boundary layers have profound effects on the flow organization (see Sakamoto & Arie 1983; Schofield & Logan 1988; Wark, Naguib & Nagib 1990; Tomkins 2001; Jacobi & McKeon 2011). The present study will focus on the perturbation effects of a single spanwise array of finite cylinders with varying spacing, due to the relative simplicity of the geometry.

The wake structure of a finite wall-mounted cylinder can be influenced by three key parameters: the aspect ratio (AR) (cylinder height/diameter, see Sumner, Heseltine & Dansereau 2004), the cylinder height with respect to the boundary layer thickness H/δ (Sakamoto & Arie 1983; Park & Lee 2002; Hain, Kähler & Michaelis 2008), and the incoming flow condition, laminar or turbulent (Wang *et al.* 2006). The present study considers cylinders of $AR = 4$ in a turbulent boundary layer, with the cylinder height being small compared with the boundary layer thickness. For $AR = 4$, the wake can include tip vortices generated by the shear layer present at the free end,

https://doi.org/10.1017/jfm.2014.185 Published online by Cambridge University Press

Kármán vortices along most of the height (comparable to the wake generated by infinite cylinders in cross-flow), and a horseshoe vortex system near the cylinder base (Williamson 1996; Simpson 2001; Wang *et al.* 2006; Dillon-Gibbons *et al.* 2007; Hain *et al.* 2008). For hemispheres and cylinders with small H/δ mounted in a turbulent boundary layer, Tomkins (2001) found an increased number of swirling structures in the wake zones, but no dominant shedding frequency.

For a spanwise array of cylinders, the array spacing must be an important parameter. Park & Lee (2003) studied the wake behind two neighbouring cylinders with $AR = 6$, $H/\delta = 0.85$, and spacings of 1–2D, where D is the cylinder base diameter. The wake showed an asymmetric vortex structure and out-of-phase vortex-shedding for the 1D case, yet a quasi-symmetric in-phase shedding pattern was observed for the 2D case. Tomkins (2001) examined flow behind two wall-mounted hemispheres separated by 1.3D embedded in the logarithmic region of a turbulent boundary layer and found significant wake interactions leading to a persistent local velocity deficit in the symmetry plane greater than that observed in a single hemisphere wake. A recent study by Pujals, Cossu & Depardon (2010) investigated single array of small-aspect-ratio cylinders with $H/\delta = 0.8$ in a turbulent boundary layer at $Re_\tau = 370$, with the spacing maintained at 4D while considering a range of diameter values from 0.75δ to 3δ. PIV measurements acquired at a height of 0.4δ revealed a sinusoidal variation in average streamwise velocity across the span that matched the array spacing (λ) and persisted far downstream (up to 8λ or 30δ). An array spacing of 6δ yielded the strongest variations in amplitude.

Prior to the present study, Ryan, Ortiz-Dueñas & Longmire (2011) performed hot-wire measurements of flow behind a single array of wall-mounted cylinders of $AR = 1.5$ (with $D^+ = 100$) in a turbulent boundary layer at $Re_\tau = 1200$. The cylinder height was $H/\delta = 0.15$ ($H^+ = 150$) such that the cylinders reached the top of the log layer. The spacings considered were 3D (0.25δ) and 6D (0.5δ), with the result that interaction between adjacent cylinder wakes occurred further downstream with increased spacing. The authors also tested cylinders with reduced diameter ($AR = 3$, $H^+ = 150$, $D^+ = 50$) and reduced diameter and height ($AR = 2$, $H^+ = 100$, $D^+ = 50$). The diameter reduction yielded weaker perturbations to RMS velocities at similar downstream distances. By contrast, RMS profiles for both H^+ values were similar up to $z^+ = 100$. At larger z^+, the $H^+ = 100$ case reverted more quickly to the unperturbed condition. Ortiz-Dueñas, Ryan & Longmire (2011) performed SPIV and volumetric three-component velocimetry (V3V) measurements in a boundary layer at $Re_\tau = 2480$ perturbed by a cylinder array with $AR = 4$ and $H/\delta = 0.2$ ($H^+ = 500$). Array spacings of 4D (0.2δ) and 8D (0.4δ) were considered, and the authors concluded that the 0.4δ spaced array produced relatively stable and persistent downstream structures while the 0.2δ case yielded rapid pairing of adjacent wakes as well as greater disorganization of individual eddies immediately downstream of the array.

1.3. *Objectives*

In the present study, the work of Ortiz-Dueñas *et al.* (2011) and Ryan *et al.* (2011) is extended to examine larger array spacings consistent with the typical spanwise packet spacing observed in previous research and to clarify the effect of the perturbations on the existing organization in the upstream flow. A Fourier transform method is applied to reveal the dominant spanwise spacing of the LMRs in the natural boundary layer (referred to as unperturbed flow) as well as in the flow downstream of perturbations. Results of both fixed and traversing PIV are employed to understand the average and instantaneous flow evolution over distances up to 7δ downstream of the perturbations.

https://doi.org/10.1017/jfm.2014.185 Published online by Cambridge University Press

U_∞	0.508 m s^{-1}
θ	12.1 mm
δ	125.5 mm
δ^*	15.9 mm
u_τ	0.0198 m s^{-1}
$Re_\tau = u_\tau \delta / \nu$	2480
$Re_\theta = U_\infty \theta / \nu$	6150

TABLE 1. Turbulent boundary layer parameters 6 m downstream of trip, as determined by Gao (2011).

2. Experiment and methods

2.1. *Facility*

The experiments were conducted in the turbulent boundary layer water channel research facility in the Department of Aerospace Engineering and Mechanics at University of Minnesota. The test section is constructed of glass plates and is 8 m long, 1.22 m wide, with a free water surface 0.39 m above the bottom wall for the present investigation. The water is driven by three propellers, and returns to the inlet from the outlet through three pipes underneath the test section. Before entering the test section, the water travels through a series of screens and honeycomb sections and then an asymmetric 5:1 contraction. The boundary layer on the bottom surface is tripped at the entrance of the test section by a 3 mm stainless steel wire, and the measurement area starts 6 m downstream. At this location, the free-stream turbulence level was measured as 1.4 %. More details on the facility and base flow can be found in Gao (2011).

A computer-controlled traversing system is mounted on top of the working section in order to perform tracking measurements. Two rails are laid on top of the side walls throughout the working section, and the traverse along the rails is driven by two motors such that it can travel in the streamwise direction at speeds of up to 1 m s^{-1} with adjustable spanwise location. A platform on the traverse holds the cameras and laser sheet optics so that measurements can be taken as the traverse moves. In order to view the flow from above, a glass interface box with a square bottom of 0.8 m $\times$ 0.8 m is installed below the traverse and the glass surface is submersed in the water by 15 mm. With the interface box mounted, the boundary layer parameters measured at 6 m downstream of the trip are given in table 1.

To study the perturbation effects on the coherent packets, a single spanwise array of stainless steel cylinders was used. The cylinder aspect ratio was $AR = 4$, with the height ($H/\delta = 0.2$, $H^+ = 500$) chosen so that each cylinder extended to the top of the log layer. The cylinders were glued to the bottom floor of the water channel 6 m downstream of the trip, and this streamwise location is defined as the origin of the x-axis. Four cylinder spacings were studied: 0.2δ, 0.4δ, 0.6δ and 0.8δ. Based on the full boundary layer thickness and span, these array spacings corresponded with area blockage ratios of 4–1 %.

2.2. *Equipment and experimental set-up*

A dual-head Spectra Physics Nd:YAG laser with an output power of 370 mJ/pulse provided illumination for PIV measurements. The laser beams first passed through a set of spherical lenses of focal length $f = 500$ mm to reduce the divergence, and a

https://doi.org/10.1017/jfm.2014.185 Published online by Cambridge University Press

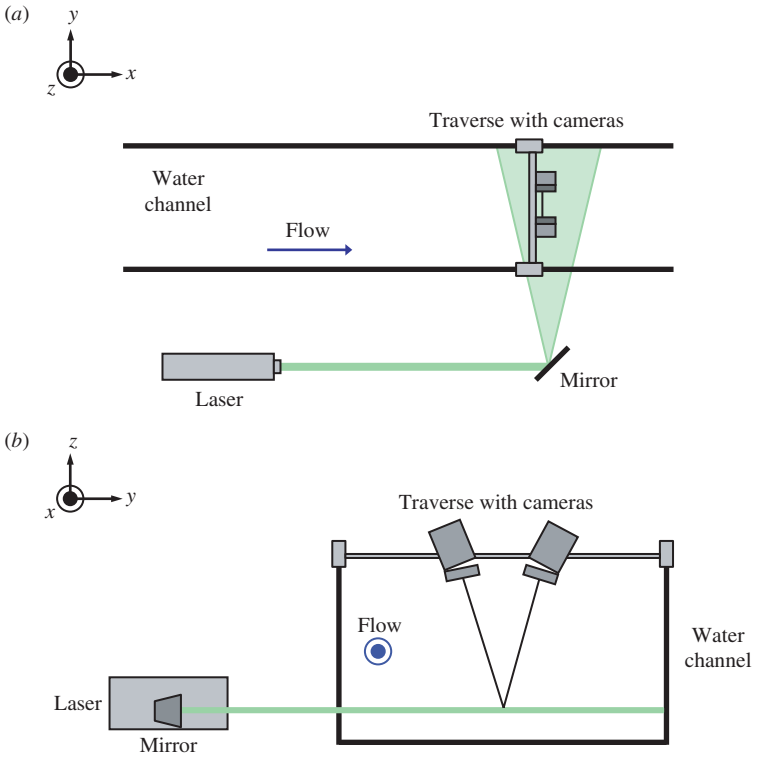


FIGURE 1. (Colour online) Schematic of the experimental set-up.

set of mirrors that coupled them to the laser sheet optics mounted on the traverse. The sheet optics included one spherical lens with $f = 1000$ mm and two convex cylindrical lenses with $f = 60$ mm. Two 12-bit TSI PowerView Plus 4MP cameras with 2048 $\times$ 2048 pixels were used along with Nikon Micro-Nikkor 60 mm lenses. The f number was chosen to be 5.6, and the magnification was approximately 0.11. Both cameras were equipped with a Scheimpflug adapter for quality imaging. The flow was seeded with silver-coated hollow glass spheres from Potters Industries LLC, with a mean diameter of 16 μm (diameter range of 6–25 μm). Particle diameters in the camera images were typically larger than 3 pixels.

A schematic of the experimental set-up is given in figure 1. The laser sheet was approximately 1 mm thick and located 15 mm ($z^+ = 300$) above the wall at the centre of the field of view (FOV). This height was chosen, based on V3V measurements by Ryan (2011), as a location at which significant spanwise periodicity in streamwise and wall-normal velocities was observed. For fixed location measurements, both SPIV and PPIV measurements were performed. For SPIV experiments, each camera was oriented at approximately 30° to the z-axis, and the FOV was approximately $1.1\delta \times 1.1\delta$. For PPIV measurements, the angle between each camera and the z-axis was reduced to $\sim$10° to minimize the overlap, yielding a layout of two side-by-side fields of view. The resultant FOV for this arrangement was $1.1\delta \times 1.9\delta$ in the x and y directions respectively. This is necessary for cases with larger cylinder spacings in order to resolve important spanwise modes.

https://doi.org/10.1017/jfm.2014.185 Published online by Cambridge University Press

2.3. *Methods*

Since the particle images were acquired through the interface box, which was submersed into the water, the tilt angle of the box due to the force from the flowing water was an important factor for the image quality and calibration. For fixed location measurements, a calibration image of a dual-plane calibration plate was taken with the channel running at $U_\infty = 0.508$ m s^{-1}. During flying measurements, the traverse moved at 0.37 m s^{-1}. Therefore the velocity difference was calculated, and the channel was set to run at $U_\infty = 0.138$ m s^{-1} while a calibration image was taken to minimize the error introduced by the interaction between the box and the water surface. A self-calibration (Wieneke 2005) was subsequently performed on all cases of stereoscopic measurements to correct the original calibration, including any effects due to misalignment between the laser sheet and calibration plane.

For the fixed SPIV and PPIV measurements, five consecutive fields from directly downstream of the cylinder array up to 4.6δ and a far field at 6.4–7.4δ were considered. An unperturbed case (with no cylinders mounted) was examined at $x/\delta = 0$. A total of 1000 image pairs were collected at each location with a sampling rate of approximately 0.5 Hz. The time difference between paired laser pulses was chosen to be $\Delta t = 800$ μs, corresponding to average particle displacements of approximately 8 pixels.

Based on the traversing system and the SPIV arrangement, a method referred to as flying PIV (FPIV) was employed to track the flow evolution in specific runs. For all FPIV experiments, the traverse was first accelerated to a fixed speed before data were acquired over a streamwise range of $-2 < x/\delta < 7$. The traversing speed (0.37 m s^{-1}) was set based on the mean velocity of the flow at the measurement height in the unperturbed case. Image pairs were captured with a sampling rate of 7.25 Hz, and an average number of 40 runs was taken for each case. The time difference between paired pulses for FPIV measurements was $\Delta t = 1800$ μs yielding average particle displacements of approximately 16 pixels.

All vector fields were calculated using DaVis 7.4 from LaVision. For all SPIV and PPIV data sets, an interrogation window size of 32 × 32 pixels was used with 50 % overlap. The resulting vector spacing was $l = 1.1$ mm ($l^+ = 21$). For FPIV measurements, the interrogation window size was chosen to be 64 × 64 pixels with 50 % overlap. This larger window size was employed in combination with a longer Δt to minimize random correlation errors. The corresponding vector spacing was consequently $l = 2.3$ mm ($l^+ = 45$).

Before a vector field was calculated, the original particle image was enhanced by subtracting the sliding background to eliminate large-scale variations in the background intensity. Because seed particle diameters varied over a range, the scattering also varied, leading to inhomogeneous particle intensities. Therefore, an intensity normalization was performed in DaVis to correct the local particle intensity. After each field was calculated, spurious vectors were removed using both a local median filter (Westerweel 1994) and a global filter. The global filter removed vectors that lay more than three standard deviations from the mean velocity. When a vector was removed, the empty cell was filled with an interpolated velocity vector.

A key effort made in this study was to quantify the spanwise spacing of the LMRs in the measurement plane. In the unperturbed flow, the LMRs are thought to be induced by coherent vortex packets, and therefore their scaling is assumed to correspond with spanwise packet scaling.

The spanwise variation of streamwise velocity at specific x locations was extracted from individual vector fields. The largest wavenumber was defined by $k_{max} = 2\pi/\Delta y$,

https://doi.org/10.1017/jfm.2014.185 Published online by Cambridge University Press

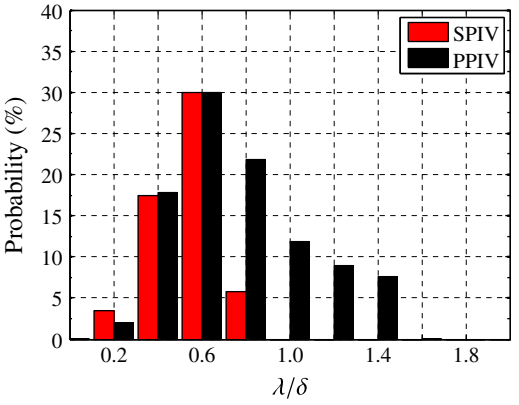


FIGURE 2. (Colour online) Distribution of dominant spanwise scales for unperturbed flow using SPIV (red) and PPIV (black). Vertical axis gives the probability scale of the PPIV result. The SPIV probability scale is normalized to match the 0.6δ mode in PPIV.

where Δy was the size of the interrogation window. Based on the Nyquist–Shannon sampling theorem, a low-pass filter was applied to eliminate components larger than $k_{max}/2$. Then, a fast Fourier transform (FFT) was performed to transform the data into the wavenumber domain, and the wavenumber component with the largest amplitude was selected. Note that the smallest wavenumber that could be detected was limited by the span of the FOV (denoted by Y) and thence only the components larger than $k_{min} = 2\pi/Y$ could be counted. For improved accuracy, a curve fit was performed surrounding the selected peak and the resulting fitted peak was identified. The wavenumber corresponding to this peak was then defined as the dominant spanwise scale for the given x location in the given vector field. The same procedure was performed at each streamwise location in each vector field, and the final results were binned into PDFs showing the distribution of dominant spanwise scales. The bin size was set to 1/10th of the spanwise FOV. More details can be found in Zheng (2013).

Figure 2 shows the result for unperturbed flow using both SPIV and PPIV set-ups. The dominant scale was detected to be approximately 0.6δ in both cases. The components smaller than 0.6δ mode agreed well, yet the 0.8δ mode yielded a great difference. This indicated the limitation of the identification method when the mode approached the spanwise limit of the FOV. Therefore, in the following section, the 0.8δ mode is discussed using the PPIV data, which had a span twice as large as the SPIV data. The detected modes beyond 1.4δ are not discussed in this paper as they suffer from underestimation.

2.4. *Experimental uncertainty*

Measurement uncertainty was introduced in several aspects. The uncertainty due to the vibration of the traversing system was estimated as 0.09 pixels when traversed at 0.37 m s^{-1} (see Gao 2011). Another part of uncertainty comes from the reconstruction method of the vector fields. Since the correlation peak uncertainty for a single vector in planar PIV is typically 0.1 pixels (Westerweel, Dabiri & Gharib 1997), based on the geometry of the present set-up and the rule of uncertainty propagation, the uncertainties for the SPIV set-up were estimated to be 0.07, 0.08 and 0.14 pixels respectively in the x, y and z directions, corresponding to 0.64, 0.73 and 1.28 % of

https://doi.org/10.1017/jfm.2014.185 Published online by Cambridge University Press

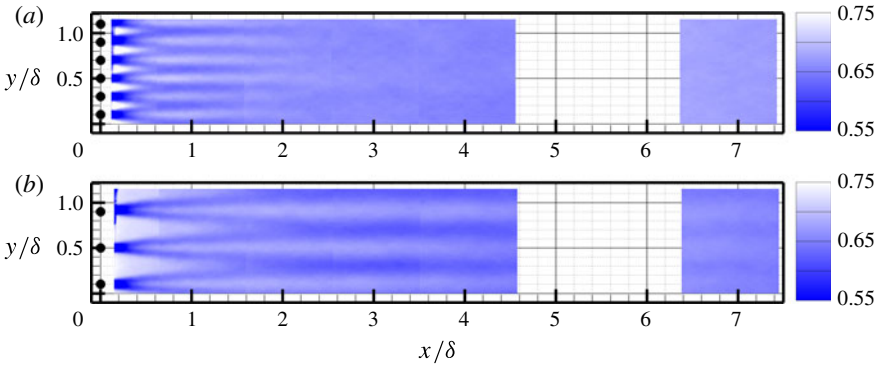


FIGURE 3. (Colour online) Averaged streamwise velocity field of the (*a*) 0.2δ case and (*b*) 0.4δ case, normalized by $U_\infty = 0.508$ m s^{-1}. Blue is slow, white is fast.

U_∞. Other than the uncertainty due to peak location, calibration uncertainties also affected the results. The fitting error of SPIV was smaller than 0.05 pixels after an iterative self-calibration process. For PPIV measurements the error was ~0.1 pixels ($0.9\,\%U_\infty$), since no self-calibration was applied and only one image was used to determine the fitting function.

The statistical uncertainties in average velocities were estimated using the unperturbed data. However, the calculated uncertainties in the mean velocity using $N = 1000$ were much smaller than those observed in the fields. It was not surprising, as we believed there were very-large-scale streamwise structures in the flow, and therefore consecutive images were probably not independent. Finally, by examining the largest deviation of the averaged velocities across the nominally homogeneous fields, the overall uncertainties in average velocity were estimated as 0.60, 0.54 and 0.73 % of U_∞, for $\overline{U}$, $\overline{V}$ and $\overline{W}$ respectively, in SPIV measurements. For PPIV measurements, the uncertainties were estimated as 1.77 and 1.30 % of U_∞, for $\overline{U}$ and $\overline{V}$ respectively.

3. Averaged results

3.1. *Averaged velocity fields*

The averaged results of perturbed cases (i.e. with the cylinder array mounted on the channel floor at $x/\delta = 0$) are presented in this section. All velocities are normalized by $U_\infty = 0.508$ m s^{-1}, and all spatial locations are normalized by δ measured at $x/\delta = 0$. Figure 3 shows the averaged streamwise velocity field for the 0.2δ and 0.4δ spacing cases, where cylinder positions are marked by large black dots at $x/\delta = 0$. Individual cylinder wakes first split, and then merge or pair with their neighbours. For the 0.2δ spacing case, the merging of split cylinder wakes happens within $x/\delta = 0.5$ downstream of the array. New slow-moving regions are formed in the mid-spacing location after the merging with a spanwise spacing of 0.2δ. These slow-moving regions remain parallel and last up to $x/\delta = 2$ before they disappear. After that, the average streamwise velocity continues to increase and no clear pattern of slow-moving regions can be observed. This suggests that the perturbation scale introduced by the cylinders either becomes distributed randomly over the span or else is no longer present in the flow. The mean velocity in the final field shown (centred on $x/\delta = 7$) is approximately 93 % of the unperturbed value at this measurement height.

https://doi.org/10.1017/jfm.2014.185 Published online by Cambridge University Press

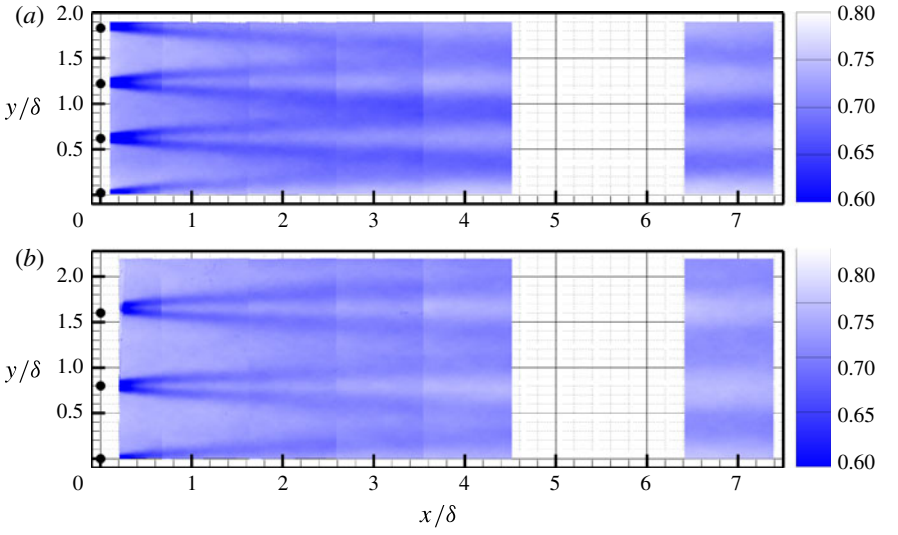


FIGURE 4. (Colour online) Averaged streamwise velocity field of the (*a*) 0.6δ case and (*b*) 0.8δ case, normalized by $U_\infty = 0.508$ m s^{-1}. Blue is slow, white is fast.

For the 0.4δ spacing case, the splitting pattern of cylinder wakes is also observed, but the subsequent merging of the split cylinder wakes happens further downstream at $x/\delta = 2$. Each wake structure interacts with the neighbouring one and settles at the mid-spacing location where slow-moving regions remain strongly organized up to $x/\delta = 4.6$, indicating weaker spanwise movement of the wakes and greater persistence compared to the 0.2δ case. In the far field at $x/\delta = 7$, a weak spanwise variation of the streamwise velocity can still be observed, with a peak-to-peak amplitude of $0.01U_\infty$. The spanwise spacing is approximately 0.4δ, which is the same as the cylinder array spacing. Therefore, we can say the downstream flow is more stable, which is consistent with Ortiz-Dueñas *et al.* (2011) and Ryan (2011).

To test the previous conclusion of Ortiz-Dueñas *et al.* (2011) that increased cylinder spacing enhanced packet stability, 0.6δ and 0.8δ spacing cases were captured using the PPIV setup, and the averaged streamwise velocity fields are shown in figure 4. Note that the contour levels are different from those in figure 3, as the flow is less obstructed by the cylinders and, therefore, a higher streamwise velocity is expected. The 0.6δ spacing case again shows the shift of wake structures towards the mid-spacing locations, with a merging at $x/\delta = 3.5$. Beyond this location, these slow-moving regions remain distinct and well organized until the end of measurement domain at $x/\delta = 7.4$. The peak-to-peak amplitude of the spanwise variation at $x/\delta = 7$ is calculated to be $0.04U_\infty$, which is four times larger than that in the 0.2δ case. Therefore the perturbation scale is well sustained.

The 0.8δ spacing case shows a similar pattern. In the averaged field, the split cylinder wakes remain distinct up to $x/\delta = 4.5$. An extrapolation suggests that they merge at the mid-spacing location at approximately $x/\delta = 5$. In the far field, we can still observe the spanwise variation of the velocity with a 0.8δ spacing, yet the variation is weaker compared to the 0.6δ case, with a peak-to-peak amplitude of $0.03U_\infty$. Therefore these results suggest that the effect of the perturbation is slightly better preserved in the 0.6δ spacing case.

https://doi.org/10.1017/jfm.2014.185 Published online by Cambridge University Press

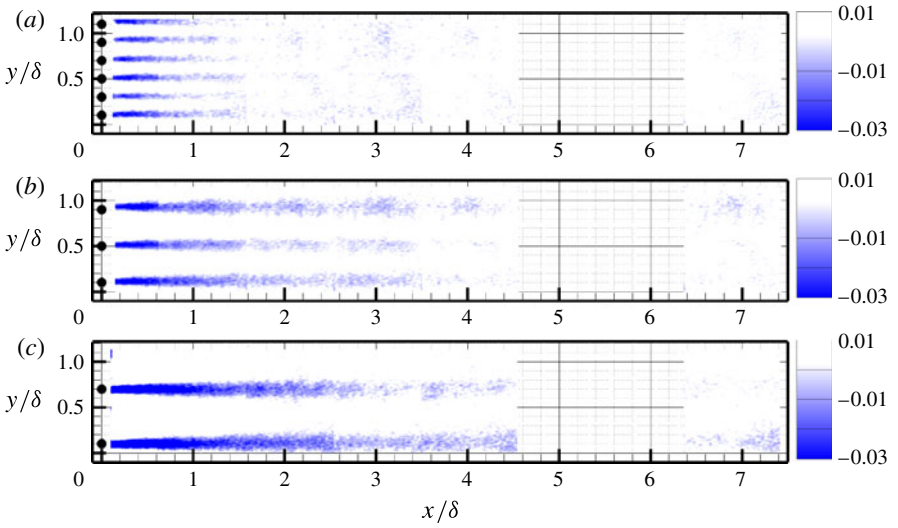


FIGURE 5. (Colour online) Averaged wall-normal velocity field of the (*a*) 0.2δ case, (*b*) 0.4δ case and (*c*) 0.6δ case, normalized by $U_\infty = 0.508$ m s^{-1} (only the downwash is shown).

Previous studies have shown downwash effects generated downstream of the free end of finite cylinders (Park & Lee 2002; Sumner *et al.* 2004; Ortiz-Dueñas *et al.* 2011). Figure 5 gives the averaged wall-normal velocity fields of the 0.2δ, 0.4δ and 0.6δ cases measured using the SPIV set-up. The most obvious observation is the downwash directly behind each cylinder. Due to this downwash motion, faster moving fluid must be carried downwards towards the bottom wall. This can be used to explain the streamwise velocity variations where a region of faster moving fluid tends to develop directly behind each cylinder. For the 0.2δ spacing case, this downwash behaviour is apparent up to $x/\delta = 1.5$, and for the 0.4δ spacing case, the downwash behaviour lasts until $x/\delta = 4$, where the spanwise variation pattern is already indistinct. For the 0.6δ spacing case, however, the downwash pattern remains distinct until at least $x/\delta = 4.6$, with some persistence throughout the measurement domain. These observations, together with the averaged streamwise velocity results, suggest that both in-plane and wall-normal velocities affect the flow organization in the measurement plane. The results are also consistent with averaged V3V measurements of Ryan (2011) that depicted alternating upwash and downwash zones and accompanying streamwise velocity downstream of 0.2δ and 0.4δ arrays. The average downwash and upwash were significant from $z^+ = 100$ to $z^+ = 500$ (or top of the cylinder).

Finally, the streamwise velocity pattern of wake splitting followed by merging looks very similar to results from Pujals *et al.* (2010) for a case with much smaller aspect ratio (0.48), larger H/δ (0.8), much larger array spacing ($\lambda = 6\delta$) and $Re_\tau = 370$. In their experiments, the results were acquired at a similar height z/H, but well into the outer region. Due to the reduced AR, the separation off of the top surfaces of the cylinders and wall-normal motions in the wake would likely be much more important than in the present flow, which supports Kármán shedding along a significant portion of the cylinder length. It is notable that the merging location of the split wakes in the Pujals flow occurs earlier in terms of the array spacing ($x/\lambda = 4$) than in the present results for the arrays with larger spacing (0.4δ–0.8δ), which yield $x/\lambda = 5$–6 such that

https://doi.org/10.1017/jfm.2014.185 Published online by Cambridge University Press

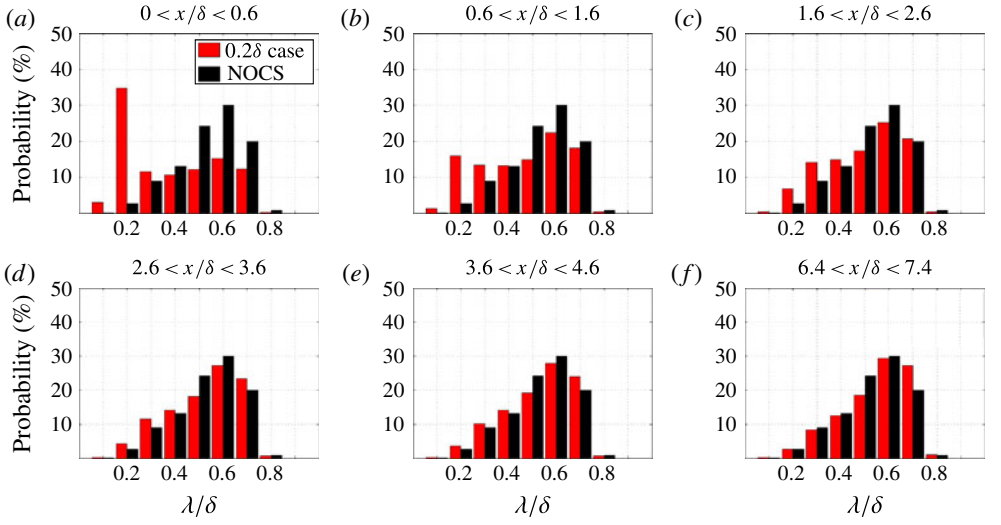


FIGURE 6. (Colour online) Spanwise scales of the 0.2δ case (red) in different fields plotted against the unperturbed case (black). NOCS represents no cylinder, stereoscopic measurement case.

the x location increases slightly with increasing array spacing. The present 0.2δ array, which exhibited early and strong spanwise interactions between neighbouring wakes, had a merging location of about 4λ, matching the Pujals result, although perhaps because of a different mechanism.

3.2. *Dominant spanwise modes*

The distributions of dominant spanwise scales of each case are based on spanwise variations in streamwise velocity with the results calculated using the Fourier method described in § 2.3.

Figure 6 shows the distribution of dominant spanwise scales downstream of the 0.2δ array. In the field immediately downstream of the cylinders ($0 < x/\delta < 0.6$), it is clear that the 0.2δ mode dominates. In the second field ($0.6 < x/\delta < 1.6$) the wake structures start to move towards the mid-spacing locations, resulting in distinct slow-moving regions, as observed in figure 3(*a*). Consequently, the local spacing between instantaneous neighbouring wakes can vary so that the dominant spanwise scale becomes less predictable, and likely explains the percentage drop of the 0.2δ mode to 16 %. It is also clear that the percentage of larger scales (0.3–0.7δ modes) has started to grow. Note that, in all three fields within $1.6 < x/\delta < 4.6$, the probability of the 0.4δ mode exceeds that of the unperturbed case, indicating that various initial wake structures with 0.2δ spacing upstream have paired. As downstream distance increases, the probability of the 0.2δ mode continuously drops while that of the 0.6δ mode increases towards the unperturbed condition. It is obvious that the perturbation scale introduced by the cylinder array is damped, and the flow structure is returning towards the unperturbed status. Finally, in the far field of $6.4 < x/\delta < 7.4$, it can be seen that the dominant spanwise mode distribution appears similar to that of the unperturbed case, yet the percentages of smaller modes (i.e. $x/\delta \leqslant 0.6$) are smaller than those of the natural case, while the 0.7δ mode has a higher percentage (the 0.8δ mode is not discussed here due to limitations of the spanwise domain). This also

https://doi.org/10.1017/jfm.2014.185 Published online by Cambridge University Press

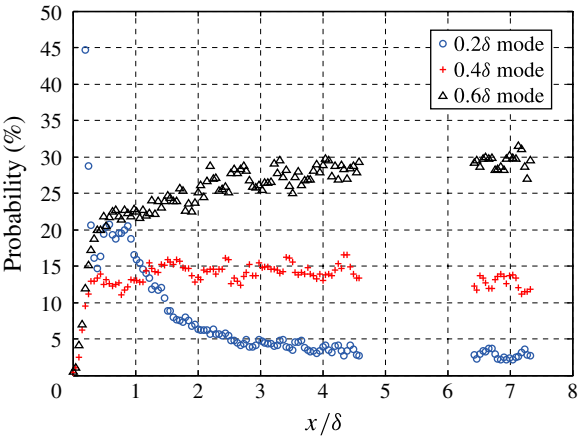


FIGURE 7. (Colour online) Streamwise development of different spanwise modes in the 0.2δ case.

suggests that the smaller spanwise scales generated by the perturbation are prone to pairing into larger scales.

The same results are presented in figure 7 to highlight the streamwise development of selected modes. Each mode is calculated within a band of $\pm 0.05\delta$, i.e. the 0.2δ mode includes values in the range 0.15–0.25δ. Note that the percentage of the 0.2δ mode starts at almost 100 % (not presented in the figure), which is reasonable considering that the perturbation scale is small enough to break down existing flow organizations in the incoming flow. There is a local minimum in the 0.2δ mode at approximately $x/\delta = 0.5$, which corresponds to the location where pairing of neighbouring wake structures begins. At this location, spanwise movements of neighbouring wakes result in scales both smaller and larger than 0.2δ. From $x/\delta = 0.5$ to $x/\delta = 1$ the percentage of the 0.2δ mode rises as some wake structures pair into new slow-moving regions. After $x/\delta = 1$, however, the 0.2δ mode gradually decreases towards the unperturbed condition. From $x/\delta =$ 4–7, it is interesting that both the 0.2δ and 0.4δ modes decrease while the 0.6δ mode increases. It is also noticeable that the probability of each mode changes more rapidly before $x/\delta = 2$, and less rapidly afterwards. This suggests that when $x/\delta < 2$ strong spanwise interactions and pairing motions are present; then as the new LMRs are formed at the mid-spacing locations, the flow becomes more stable so that the dominant spanwise scales relax more gradually towards the unperturbed condition.

Figure 8 shows the dominant spanwise scales of the 0.4δ case at different streamwise locations. The 0.4δ mode dominates the near field ($0 < x/\delta < 0.6$), and the 0.2δ mode is also elevated compared with the unperturbed case. For $0.6 < x/\delta < 1.6$, the 0.4δ mode drops off sharply, as this is the location where major spanwise movement occurs (see figure 3*b*), resulting in a broader distribution of dominant scales around 0.4δ. At this location, the probability of both smaller and larger modes, other than the 0.2δ mode, has increased compared to their counterparts in the first field.

The percentage of the 0.4δ mode next increases for $1.6 < x/\delta < 3.6$ which corresponds to the more frequent slow-moving regions in the mid-spacing locations as observed in the mean field starting at $x/\delta = 2$ (see figure 3*b*). Beyond this streamwise location, the 0.4δ mode decreases towards the unperturbed condition. In the far

https://doi.org/10.1017/jfm.2014.185 Published online by Cambridge University Press

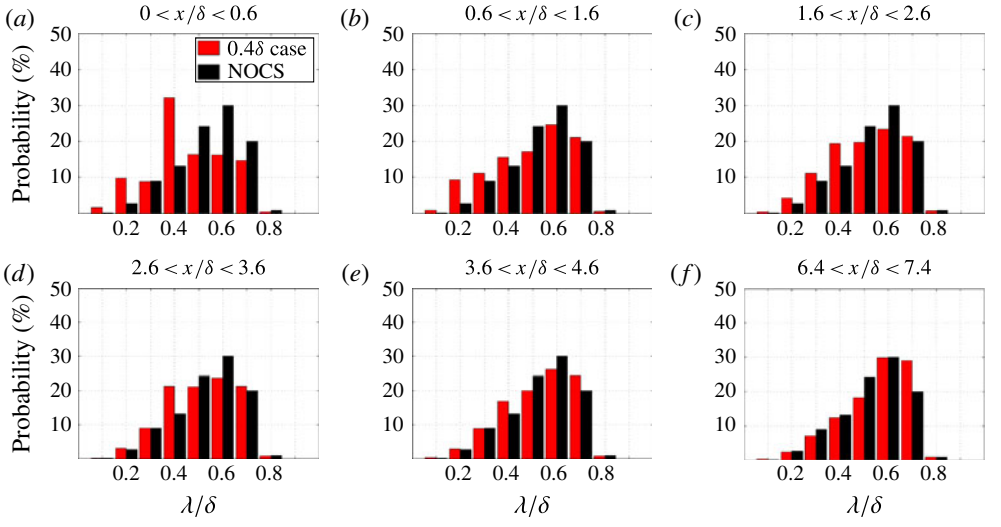


FIGURE 8. (Colour online) Spanwise scales of the 0.4δ case (red) in different fields plotted against the unperturbed case (black). NOCS represents no cylinder, stereoscopic measurement case.

field of $6.4 < x/\delta < 7.4$, the percentage of the 0.4δ mode is slightly smaller than that in the unperturbed case, yet in figure 3(*b*) a spanwise variation of the average streamwise velocity is still observed with a scale of 0.4δ. The averaged result is thus interpreted as a more repeatable spanwise location of the 0.4δ mode compared to the unperturbed case. Also, although it is difficult to resolve larger spanwise modes with this FOV, it is interesting that the 0.7δ mode is significantly higher in the perturbed case, suggesting that some 0.4δ scaled structures have paired.

The corresponding streamwise development of the dominant spanwise scales is shown in figure 9. The 0.4δ mode starts at 55 %, followed by a local minimum at $x/\delta = 0.7$, which is the same location of local peaks in the 0.2δ and 0.6δ modes. This corresponds to spanwise movements of neighbouring wake structures whereby both larger and smaller scales become more frequent. Also, the crossing of the 0.2δ and 0.4δ mode curves at $x/\delta = 0.7$, and that of the 0.4δ and 0.6δ mode curves at $x/\delta = 3$ suggest the spanwise scale growth as the flow moves downstream. After $x/\delta = 3$, the 0.4δ mode starts to decay while the 0.6δ mode rises, suggesting an increase of the dominant spanwise scale.

The distribution of dominant spanwise scales in the 0.6δ case is shown in figure 10. Note that the spanwise FOV of the figure is now 2δ, with the bin width set to 0.2δ. The most significant characteristic of these plots is that the percentage of the 0.6δ mode remains the highest in all downstream fields. Its probability drops only in the second and third fields, where spanwise movement is present based on the observation of the averaged field, yet the lowest percentage (in $0.6 < x/\delta < 1.6$) is still no less than the unperturbed case, suggesting that the spanwise scale change (and consequently spanwise interaction) is weak. In the far field $6.4 < x/\delta < 7.4$, the percentage of the 0.6δ mode is still 5 % larger than in the unperturbed case, showing that the perturbation scale introduced into the flow is well preserved throughout the measurement domain. The 0.2δ and 0.4δ modes decrease monotonically with increasing downstream distance, while the larger modes (0.8–1.4δ) increase. This

https://doi.org/10.1017/jfm.2014.185 Published online by Cambridge University Press

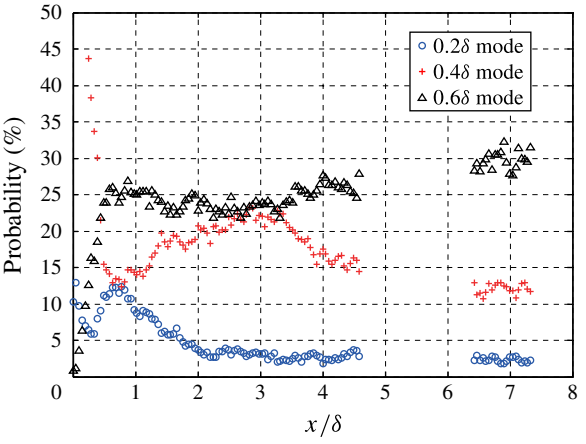


FIGURE 9. (Colour online) Streamwise development of different spanwise modes in the 0.4δ case.

again suggests that the dominant spanwise scales increase, but in this case the change is considered fairly insignificant as the shapes of the distributions are similar. In this sense, we conclude that the downstream flow organization is more stable than for the 0.2δ and 0.4δ arrays.

The streamwise development of the dominant spanwise scales is given in figure 11 for the 0.6δ case. As the measurement span is wider, the 0.8δ mode can be captured, and therefore it is added to the plot. The 0.6δ mode starts off at approximately 50 % and drops to a local minimum at $x/\delta = 1$, which is also a local maximum of the 0.4δ and 0.8δ modes due to the average spanwise shift of the slow-moving regions. After this location, the 0.2δ mode remains at a very low percentage, thence insignificant in this case, and the 0.4δ and 0.8δ modes decrease. From $x/\delta = 4$–7, note that the percentages of the 0.2δ, 0.4δ and 0.8δ modes remain almost unchanged, supporting the idea of a relatively persistent flow organization over this range.

Figure 12 shows the distribution of dominant spanwise scales of the 0.8δ case in different locations. Based on the averaged velocity field, where a visible spanwise variation of streamwise velocity is observed at $x/\delta = 7.4$ and this figure, in which the 0.8δ mode dominates most of the fields, the flow organization downstream of this perturbation also appears persistent.

In figure 13, we can see that the 0.4δ, 0.6δ and 0.8δ modes are all significant in the range $x/\delta = 2$–4, where major spanwise movements take place corresponding to the averaged field in figure 4(*b*). Other than the 0.2δ mode, which is insignificant, the three larger scale modes fluctuate over the range, and from $x/\delta = 4$ to 7, the 0.4δ mode drops significantly. At $x/\delta = 7$, although the 0.8δ mode dominates the 0.6δ mode, the percentage of the latter is still relatively large.

To better compare the four perturbation cases, only the characteristic modes (the dominant flow scale that matches the perturbation scale, i.e. the 0.2δ mode for the 0.2δ case) are plotted in figure 14 showing the streamwise development. The probability is normalized such that one matches the probability of the same mode in the unperturbed case. The 0.2δ curve starts at 35, and then drops sharply after $x/\delta = 1$ towards a value of 1. Only the 0.6δ and 0.8δ modes rise in the second half of the measurement domain; in the far field ($x/\delta = 6.4$–7.4), we can see that both of these modes remain well above one. The 0.2, 0.4, 0.6 and 0.8δ characteristic

https://doi.org/10.1017/jfm.2014.185 Published online by Cambridge University Press

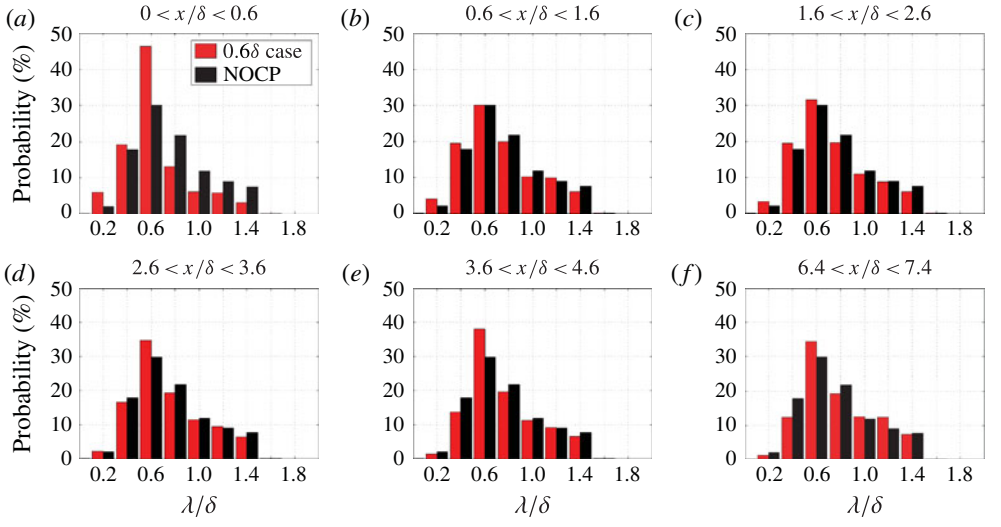


FIGURE 10. (Colour online) Spanwise scales of the 0.6δ case (red) in different fields plotted against the unperturbed case (black). NOCP represents no cylinder, planar measurement case.

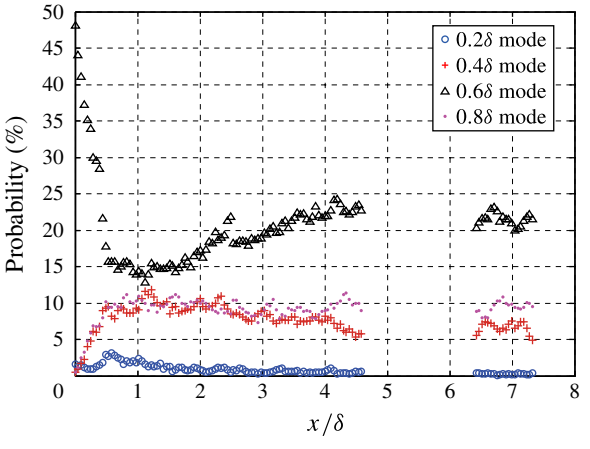


FIGURE 11. (Colour online) Streamwise development of different spanwise modes in the 0.6δ case.

modes yielded normalized probabilities of 1.02, 0.94, 1.45 and 1.32 respectively in this range for the respective perturbation cases. This suggests that both the 0.6δ and 0.8δ arrays have a long-lasting effect on the flow structures, with the 0.6δ case being relatively stronger. This might be expected given that the dominant spanwise scale of the unperturbed flow is 0.6δ.

4. Instantaneous and flying PIV results

Both fixed location and flying results are considered in this section. Figure 15 shows a random instance for the unperturbed case from fixed location SPIV measurements. In figure 15(*a*), the *Q*2 events appear strongly coherent and correlate well with the LMRs,

https://doi.org/10.1017/jfm.2014.185 Published online by Cambridge University Press

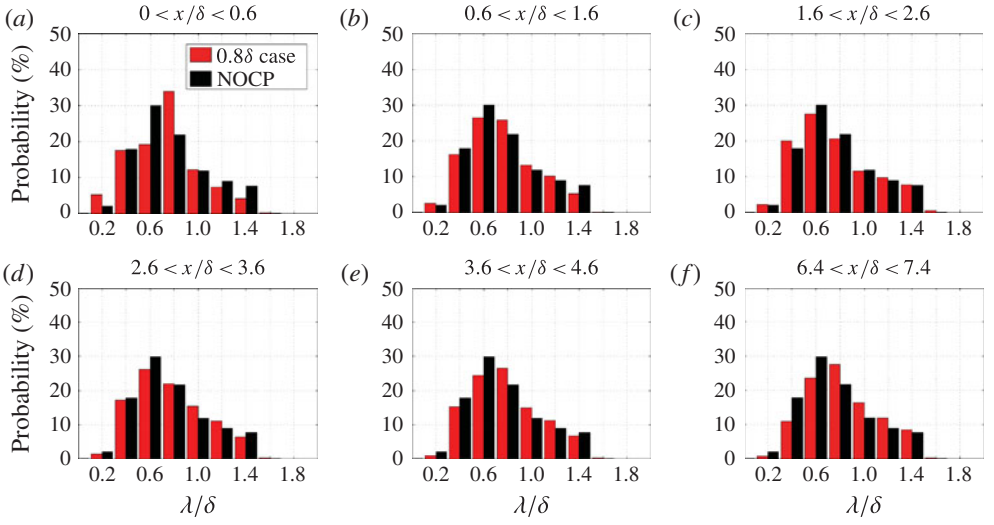


FIGURE 12. (Colour online) Spanwise scales of the 0.8δ case (red) in different fields plotted against the unperturbed case (black). NOCP represents no cylinder, planar measurement case.

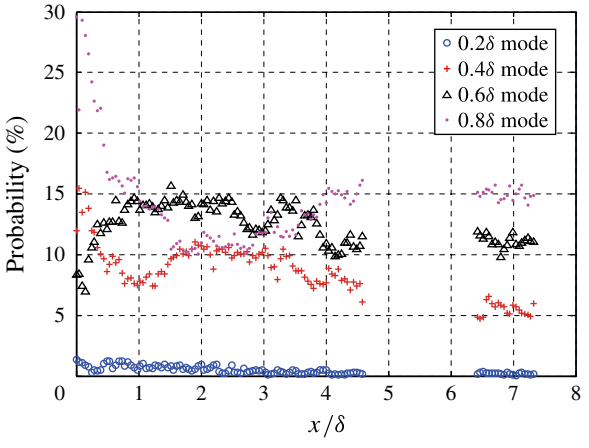


FIGURE 13. (Colour online) Streamwise development of different spanwise modes in the 0.8δ case.

which is consistent with Dennis & Nickels (2011*b*). In figure 15(*b*), negative wall-normal velocity appears significant on each side of the LMRs, which might result from the $Q4$ (sweep) events induced by the hairpin legs (see Adrian 2007). Note that the negative wall-normal velocity occurs more frequently than the $Q4$ events, suggesting that some downward flows are associated with slower streamwise velocity.

Results from one FPIV run for the unperturbed flow are given in figure 16, which shows the streamwise velocity contours and 2D swirling strength described by Zhou *et al.* (1999), signed by ω_z, as well as the Reynolds stress corresponding to $Q2$ ejections. Contour levels are set to highlight the slow-moving regions, and thence the packets. The specific threshold for 2D swirling strength was chosen to visualize

https://doi.org/10.1017/jfm.2014.185 Published online by Cambridge University Press

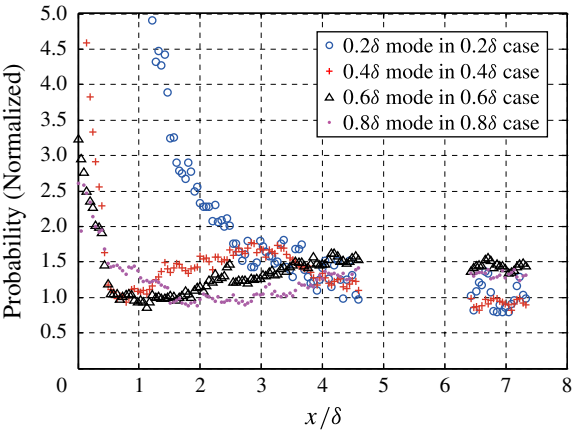


FIGURE 14. (Colour online) Streamwise development of normalized characteristic dominant spanwise scales.

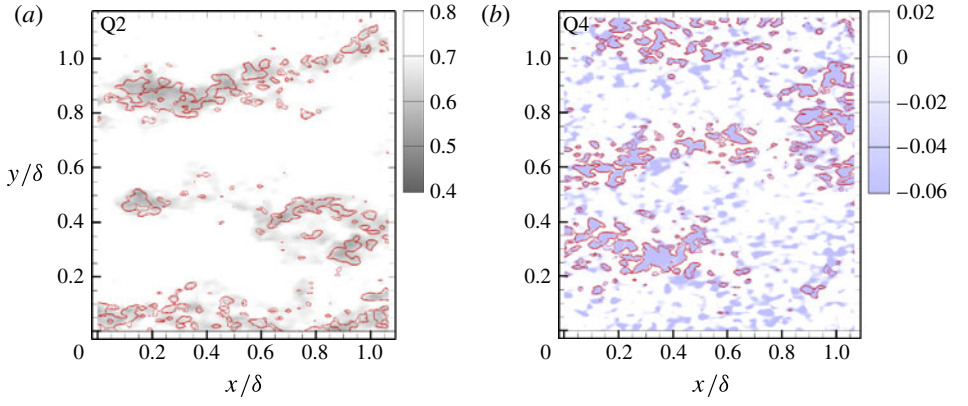


FIGURE 15. (Colour online) SPIV result for unperturbed flow. (*a*) Grey scale shows streamwise velocity normalized by $U_\infty = 0.508$ m s^{-1}, red contour line shows $Q2 = 0.5\sigma_u\sigma_w$ (σ_u and σ_w represent the standard deviation of u and w components respectively). (*b*) Blue scale shows negative wall-normal velocity normalized by $U_\infty = 0.508$ m s^{-1}, red contour line shows $Q4 = 0.5\sigma_u\sigma_w$.

individual swirling structures. The streamwise velocity is computed relative to the averaged mean velocity without the cylinders, so zero in the plot is equivalent to 0.37 m s^{-1}.

The figure shows two distinct packets identified by long LMRs surrounded by counter-rotating swirling structures coincident with zones of $Q2$ Reynolds stress. These packets persist over a streamwise range greater than 9δ (and time greater than $12.4\delta/U_\infty$). During this time, the spanwise spacing between the two packets varies over the range 0.4–0.7δ due to spanwise tilting, as observed in the last four frames. This tilting is comparable to the meandering feature observed in single time steps of DNS data by Hutchins & Marusic (2007). By contrast, we provide here a Lagrangian view of the development. To better quantify the persistence and movement of the packets over time, cross-correlations were performed between the first field and three

https://doi.org/10.1017/jfm.2014.185 Published online by Cambridge University Press

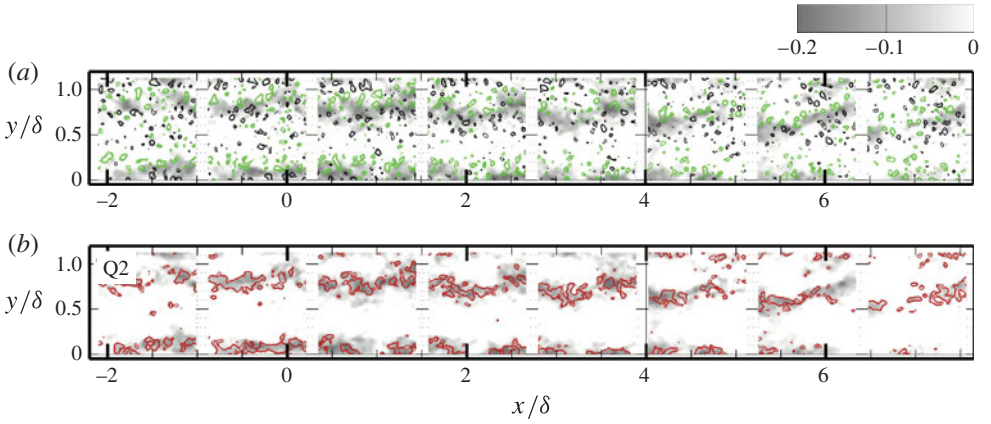


FIGURE 16. (Colour online) Selected run of the unperturbed case. Consecutive fields are separated by 0.4 s or $1.6\delta/U_\infty$. Grey scale maps the streamwise velocity relative to 0.37 m s^{-1} normalized by $U_\infty = 0.508$ m s^{-1}. 2D swirling strength is marked by contour lines (black: $\lambda_{ci} > 0.6$, green: $\lambda_{ci} < -0.6$, signed by ω_z). High Reynolds stress ($-uv$) $Q2$ regions are marked by red contour lines ($Q2 = 0.5\sigma_u\sigma_w$).

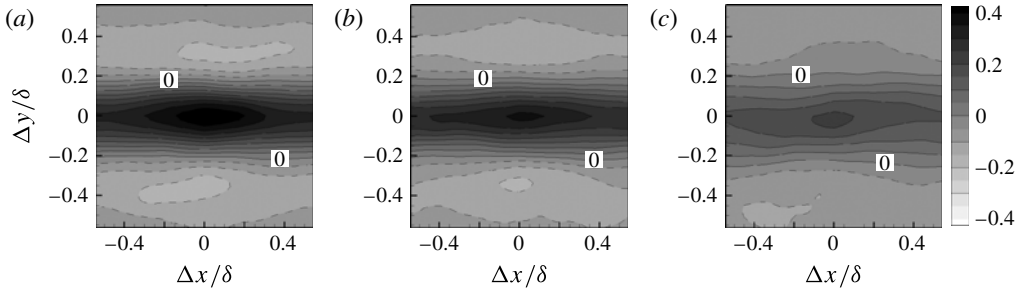


FIGURE 17. Unperturbed flow. Cross-correlation map of streamwise velocity between the first and (*a*) third, (*b*) fourth and (*c*) eighth FOV averaged over 40 runs. Here Δx and Δy give the relative displacement between image centres in the x and y directions respectively.

selected downstream fields of streamwise velocity in each run, and the results were averaged over all 40 runs, as shown in figure 17. Note that figure 17(*a*) yields a correlation shape that is very similar to the auto-correlation, and consistent with previous results of Ganapathisubramani *et al.* (2005). The overall correlation value decreases as correlation pair distance (time) increases, which could possibly result from spanwise movement and tilting of packets, out-of-plane motions, or evolution of other flow features. Also, these and additional intervening correlations show that the spanwise half width (length scale from the centre to the zero contour line) increases from 0.17 to 0.21δ with increasing separation time. The negative tails of the curves also show that, on average, the spanwise periodicity is generally larger than 0.56δ, which is consistent with the Fourier results discussed earlier.

4.1. *Strong perturbation:* 0.2δ *spacing*

Since the narrowest array spacing of 0.2δ provides the strongest flow obstruction, we refer to that case as a strong perturbation. Figure 18 gives an example of flow

https://doi.org/10.1017/jfm.2014.185 Published online by Cambridge University Press

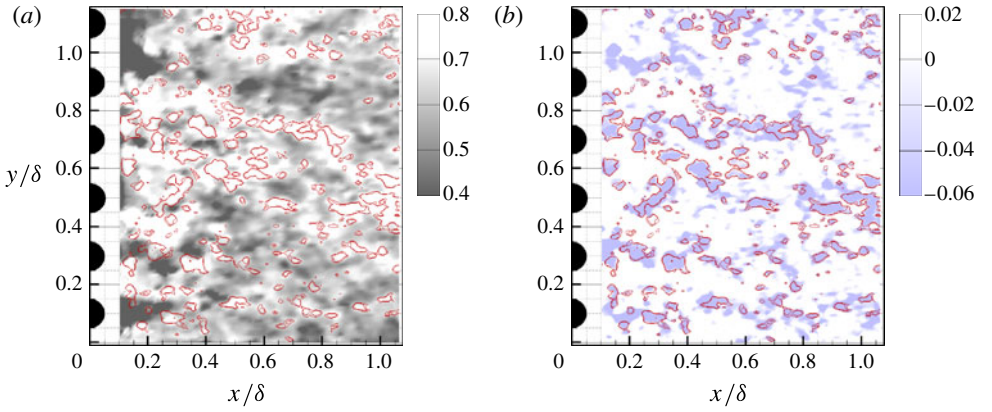


FIGURE 18. (Colour online) Instantaneous SPIV measurement from the 0.2δ spacing case. (*a*) Grey scale shows streamwise velocity and red contour lines give $Q4$ events. (*b*) Blue scale shows negative wall-normal velocity and red contour lines give $Q4$ events. Black dots give cylinder locations. Velocities are normalized by $U_\infty = 0.508$ m s^{-1} and $Q4 = 0.5\sigma_u\sigma_w$.

immediately downstream of the array, showing both streamwise and wall-normal velocity along with $Q4$ events. The $Q4$ events are located most frequently directly behind the cylinders, suggesting that tip downwash brings faster moving fluid to the measurement plane. In figure 18(*b*), the downwash zones behind the top two cylinders interacted with each other, while the zones behind the bottom two cylinders remained independent. This suggests a strong spanwise interaction between the cylinder wakes, and consequently an unorganized downstream flow, which is consistent with previous discussions. Note that a Kármán-like shedding pattern is observed behind the cylinder at $y/\delta = 0.3$ in figure 18(*b*), which is also frequently observed in other instances. This makes sense because, based on $Re_D = 2340$, the observed shedding Strouhal number is $\sim$0.2, and for the present cylinders, with $AR = 4$, Kármán shedding patterns could be expected (see Sumner *et al.* 2004).

Figure 19 gives two selected FPIV runs of the 0.2δ spacing case. The first shows two distinct packets in the incoming flow, as indicated by the well-aligned swirl structures along the streamwise direction on both sides of the LMRs. Immediately downstream of the cylinders, the streamwise velocity is greatly decreased, and neighbouring wake structures interact. Consequently the number of swirl structures increases. The incoming vortex packets appear to be broken down to smaller scales, at least at this measurement height. The individual vortices interact with spanwise neighbours so that the flow appears very disorganized up to approximately $x/\delta = 2$. Then the swirling structures start to reorganize themselves towards the status seen in the incoming flow, i.e. two independent LMRs are observed at $x/\delta = 2$, and their spanwise spacing and location are similar to those of the upstream packets.

The bottom sequence shows three possible incoming packets in the upstream flow (two stronger ones on top and a weak one on the bottom), and the obstructed packets seem also to reappear near $x/\delta = 2$. In the far field, we can observe two LMRs surrounded by well-aligned swirls, and in the bottom possibly a very weak LMR with some counter-rotating swirls on each side, which corresponds to the weak incoming packet.

Both of these runs show that the far-field packet organization corresponds to the upstream packet organization, and similar instances were observed frequently in the

https://doi.org/10.1017/jfm.2014.185 Published online by Cambridge University Press

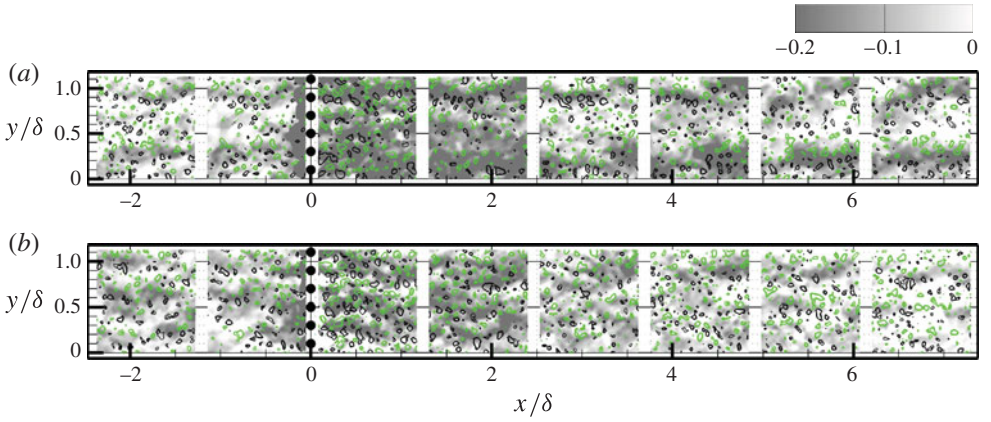


FIGURE 19. (Colour online) Two selected runs of the 0.2δ spacing case. Consecutive fields are separated by 0.4 s or $1.6\delta/U_\infty$. Grey scale maps the streamwise velocity relative to 0.37 m s^{-1} normalized by $U_\infty = 0.508$ m s^{-1}. 2D swirling strength is marked by contour lines (black: $\lambda_{ci} > 0.6$, green: $\lambda_{ci} < -0.6$, signed by ω_z).

0.2δ case. Cross-correlations were performed for this case using the same method mentioned above for the same streamwise fields, as shown in figure 20. The averaged result between the furthest upstream field and the field immediately downstream of the cylinder array is shown in figure 20(*a*). This correlation is much weaker (maximum value of 0.15) compared with the corresponding unperturbed case in figure 17(*a*) (maximum value of 0.45). This weak correlation results from the breakdown of the incoming packet organization and the sudden presence of interacting cylinder wakes. The negative lobes bounded by zero contour lines on the upper and lower edges of the plot suggest a strong spanwise periodicity in the flow, which is not observed in the correlation for the unperturbed case. In figure 20(*b*), however, which corresponds with the region where upstream packets reappear, the correlation becomes stronger. Specifically, both the shape and correlation values look similar to the unperturbed case in figure 17(*b*) (maximum values are 0.37 and 0.34 for unperturbed and perturbed flow respectively). In figure 20(*c*), where the last field is correlated with the first, the high-correlation region extends in the streamwise direction, which indicates possibly that the structures are more constrained in the streamwise direction, and possibly that their spanwise movements or tilting behaviours are more limited. The spanwise limitation of the negative lobes again suggests the spanwise periodicity in the flow. For this case, as in the unperturbed flow, the spanwise half-width also increases monotonically after the 1*3 correlation pair (first and third field in the streamwise direction).

These results suggest that although the cylinder array perturbs the vortex packets in the log layer, the packet structure remains in the outer region and drives the flow evolution as it moves downstream. This is consistent with the results of Hutchins & Marusic (2007), who suggested the possibility of large-scale packets having a significant imprint on the near-wall region.

4.2. *Weaker perturbations: wake-packet interactions*

For the larger cylinder spacings of 0.4δ and 0.6δ, the flow is less obstructed, and individual cylinder wakes are more independent. Sample fixed location measurements of the near field for these two cases are shown in figures 21 and 22 respectively. The

https://doi.org/10.1017/jfm.2014.185 Published online by Cambridge University Press

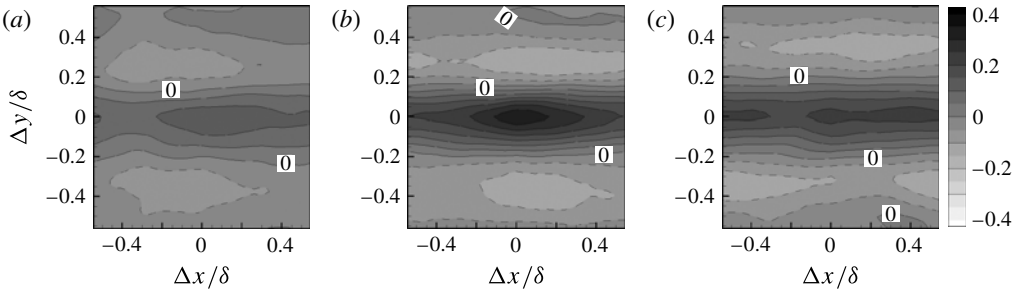


FIGURE 20. 0.2δ case. Cross-correlation map of streamwise velocity between the first and (*a*) third, (*b*) fourth and (*c*) eighth FOV averaged over 40 runs. Here Δx and Δy give the relative displacement between image centres in the x and y directions respectively.

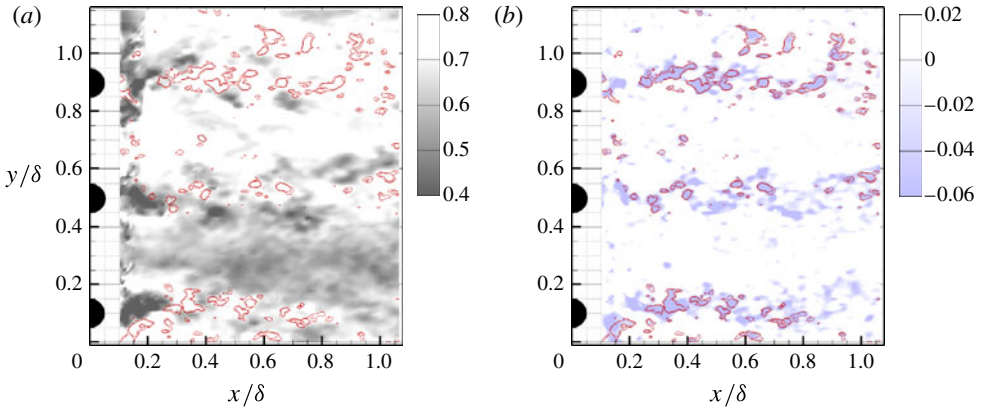


FIGURE 21. (Colour online) Instantaneous SPIV measurement from the 0.4δ spacing case. (*a*) Grey scale shows streamwise velocity and red contour lines give $Q4$ events. (*b*) Blue scale shows negative wall-normal velocity and red contour lines give $Q4$ events. Black dots give cylinder locations. Velocities are normalized by $U_\infty = 0.508$ m s^{-1} and $Q4 = 0.5\sigma_u\sigma_w$.

number of $Q4$ events is obviously smaller than in the 0.2δ case, and these events are concentrated directly behind each cylinder. Both the streamwise and wall-normal wake structures appear independent of spanwise neighbours through this FOV. Similar to the 0.2δ spacing case, Kármán-like shedding patterns are frequently observed in the 0.4δ and 0.6δ spacing cases. One example can be seen in the downwash pattern behind the middle cylinder in figure 21(*b*). Note also that in figure 21(*a*), a large LMR is observed passing between the bottom two cylinders. This suggests that the incoming flow condition affects the downstream flow development.

Based on examination of many runs, we conclude that the instantaneous downstream flow organization depends significantly on the upstream flow conditions for these larger spacing cases, and therefore all runs are classified into one of three scenarios to explain the wake-packet interactions. In the first scenario, no distinct packets were observed in the incoming flow, and individual cylinder wakes merged or paired into new slow-moving regions at spanwise locations midway between the cylinders. In the second scenario, packets in the incoming flow passed between neighbouring cylinders

https://doi.org/10.1017/jfm.2014.185 Published online by Cambridge University Press

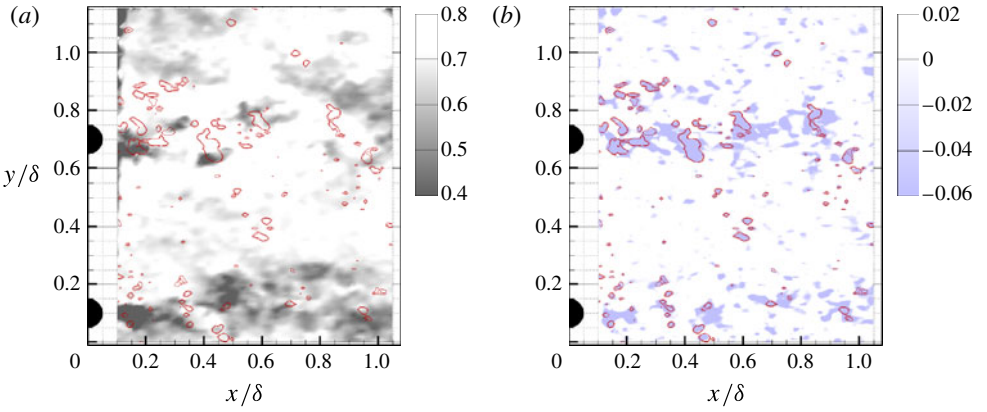


FIGURE 22. (Colour online) Instantaneous SPIV measurement from the 0.6δ spacing case. (*a*) Grey scale shows streamwise velocity and red contour lines give $Q4$ events. (*b*) Blue scale shows negative wall-normal velocity and red contour lines give $Q4$ events. Black dots give cylinder locations. Velocities are normalized by $U_\infty = 0.508$ m s^{-1} and $Q4 = 0.5\sigma_u\sigma_w$.

Scenario(s)	0.4δ case	0.6δ case
I	13 %	10 %
II	23 %	45 %
III	20 %	26 %
II and III	44 %	19 %

TABLE 2. Occurrence probabilities of different scenarios for the 0.4δ and 0.6δ spacing cases.

and attracted the nearest wake so that the existing LMRs were strengthened and remained coherent in the mid-spacing locations. In the third scenario, the incoming packets impinged directly on the cylinders. The packets were enhanced by the coincident cylinder wakes before shifting gradually towards the mid-spacing locations. Occurrence probabilities of different scenarios are given in table 2. The dominant scenarios for the 0.4δ and 0.6δ spacing cases are a combination of Scenarios II and III and Scenario II respectively. This is reasonable given that the dominant spanwise spacing of the LMRs is 0.6δ. Thus, in the 0.4δ spacing case the relative locations of neighbouring LMRs approaching neighbouring cylinders are likely to be different, while in the 0.6δ spacing case the relative locations are frequently the same. That the probability of Scenario II dominates Scenario III for 0.6δ spacing is also expected due to the relative sparsity of cylinders across the span.

4.2.1. *Scenario I*

Figure 23 shows Scenario I in the 0.4δ and 0.6δ cases, where the relatively disorganized swirling structures upstream of the cylinders indicate no strong incoming packets. No obvious interactions between cylinder wakes are observed in the near field ($x/\delta < 0.5$) because the black and green swirl contours are well aligned on each side of the individual wakes. This observation is different from the 0.2δ case,

https://doi.org/10.1017/jfm.2014.185 Published online by Cambridge University Press

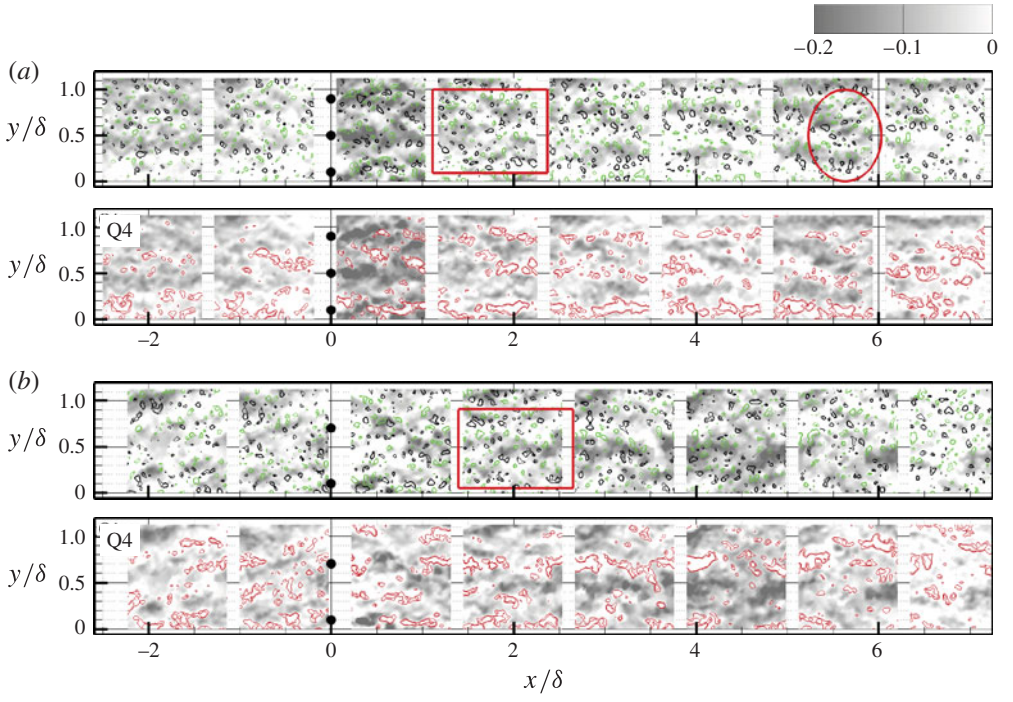


FIGURE 23. (Colour online) Selected runs of the (*a*) 0.4δ and (*b*) 0.6δ spacing cases representing Scenario I of wake-packet interaction. Consecutive fields are separated by 0.4 s or $1.6\delta/U_\infty$. Grey scale maps the streamwise velocity relative to 0.37 m s^{-1} normalized by $U_\infty = 0.508$ m s^{-1}. 2D swirling strength is marked by contour lines (black: $\lambda_{ci} > 0.6$, green: $\lambda_{ci} < -0.6$, signed by ω_z). High Reynolds stress ($-uv$) $Q4$ regions are marked by red contour lines ($Q4 = 0.5\sigma_u\sigma_w$). Red boxes mark new LMRs merged from adjacent cylinder wakes. Red ellipse marks two LMRs interacting in the far field.

where interaction between wakes began immediately downstream of the cylinders. In the 0.4δ run, some mixing of oppositely signed swirl structures can be observed throughout the span starting at $x/\delta = 1$, suggesting some spanwise interaction. Then, at $x/\delta = 2$, two independent LMRs with associated counter-rotating swirl zones (marked by the red box in figure 23*a*) are observed at the mid-spacing locations. By observing the traces of the black and green swirls, it is evident that the new LMRs result from merging parts of neighbouring cylinder wakes. These two LMRs maintain a relatively constant spacing of 0.4δ before a secondary spanwise interaction occurs at $x/\delta = 5.7$ (marked by the large red ellipse). It is unclear beyond this point whether the packets decay, merge or move out of plane. In the 0.6δ run, parts of two adjacent wakes also merge into a distinct LMR at $x/\delta = 2$ in the mid-spacing location (marked by the red box in figure 23*b*). This LMR also appears to decay at the end of the run. For this scenario, eventual decay or disappearance of LMRs initiated downstream of the 0.4δ or 0.6δ arrays occurred roughly 18 % of the time (averaging over all incoming scenarios, the percentage of existing or newly formed LMRs disappearing downstream of the 0.4δ or 0.6δ arrays was about the same at 20 %).

In this scenario of larger spanwise spacing with no distinct incoming packets, the tip downwash effects become more obvious in determining the behaviour of the cylinder wakes. In figure 23, strong $Q4$ Reynolds stress events are observed starting

https://doi.org/10.1017/jfm.2014.185 Published online by Cambridge University Press

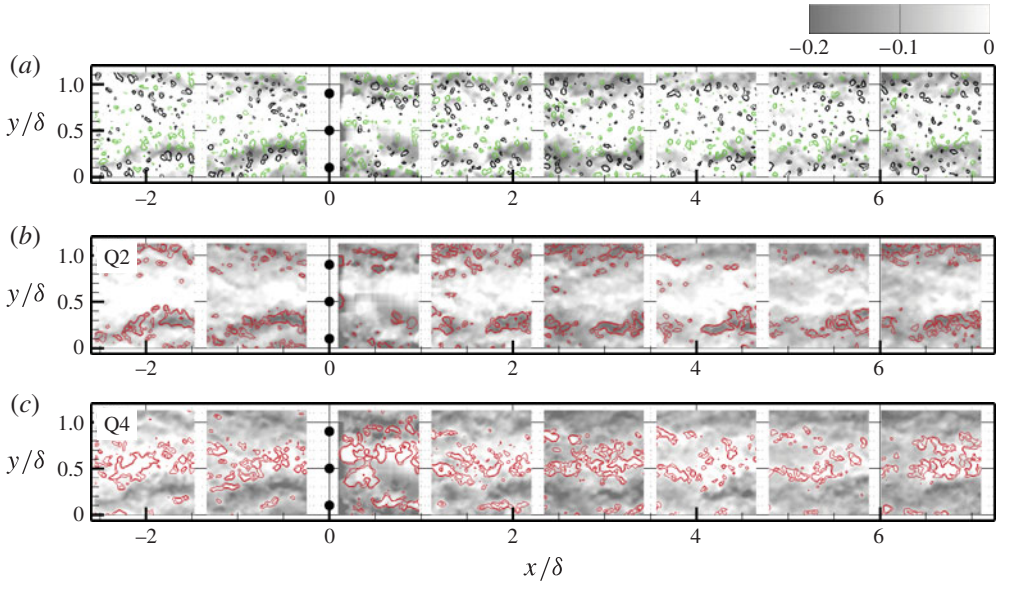


FIGURE 24. (Colour online) Selected run of the 0.4δ spacing case representing Scenario II of wake-packet interaction. Consecutive fields are separated by 0.4 s or $1.6\delta/U_\infty$. Grey scale maps the streamwise velocity relative to 0.37 m s^{-1} normalized by $U_\infty =$ 0.508 m s^{-1}. 2D swirling strength is marked by contour lines (black: $\lambda_{ci} > 0.6$, green: $\lambda_{ci} < -0.6$, signed by ω_z). High Reynolds stress ($-uv$) regions of both $Q2$ and $Q4$ events are marked by red contour lines ($Q2 = Q4 = 0.5\sigma_u\sigma_w$).

0.5δ downstream of the cylinders. Based on continuity, the slow-moving regions are expected to shift aside with possible associated upwash. These movements may also contribute to the streamwise vorticity observed by Ortiz-Dueñas *et al.* (2011) and Ryan (2011).

4.2.2. *Scenario II*

Figure 24 shows Scenario II for 0.4δ spacing where two packets present in the incoming flow are aligned approximately with the mid-spacing locations. In this case, the nearest slow-moving cylinder wakes are attracted immediately by each packet. Then each packet stays strongly coherent at the mid-spacing location throughout the measurement domain. The contours of $Q2$ Reynolds stress are focused within the packets and remain strongly coherent throughout the measurement domain. The top and bottom cylinder in the plot also appear to induce $Q4$ events starting at $x/\delta = 1$. The $Q4$ distribution downstream of the central cylinder is initially more dispersed, but then appears to align behind the cylinder starting at $x/\delta = 1$. Interestingly, the spacing between the downstream packet structures remains at 0.8δ.

Figure 25 gives an example of Scenario II in the 0.6δ spacing case. In this run, the wake of the upper cylinder shown splits, and the upper part remains distinct and independent until $x/\delta = 5$. The lower part of the wake is ingested immediately downstream of the array by the packet passing between the cylinders. The swirl structures show clear evidence of the wake merging laterally into the packet (as marked by the red ellipse). After the merging, the LMR again settles at the mid-spacing location and remains coherent to the end of the measurement domain. It is obvious that the population and strength of $Q2$ events in the LMR

https://doi.org/10.1017/jfm.2014.185 Published online by Cambridge University Press

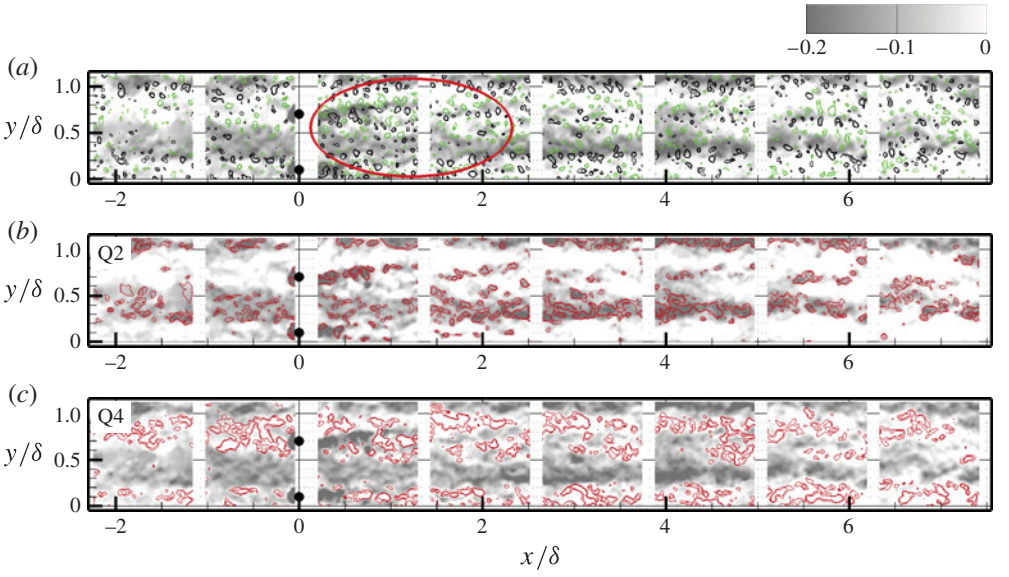


FIGURE 25. (Colour online) Selected run of the 0.6δ spacing case representing scenario II of wake-packet interaction. Consecutive fields are separated by 0.4 s or $1.6\delta/U_\infty$. Grey scale maps the streamwise velocity relative to 0.37 m s^{-1} normalized by $U_\infty =$ 0.508 m s^{-1}. 2D swirling strength is marked by contour lines (black: $\lambda_{ci} > 0.6$, green: $\lambda_{ci} < -0.6$, signed by ω_z). High Reynolds stress ($-uv$) regions of both $Q2$ and $Q4$ events are marked by red contour lines ($Q2 = Q4 = 0.5\sigma_u\sigma_w$). Red ellipse marks the splitting of the cylinder wake and the merging of lower part into the neighbouring packet.

is increased after the ingestion of the cylinder wake at $x/\delta = 2$, compared with the earlier locations. The $Q4$ events induced by the lower cylinder in this run seem to modulate the packet structure by bringing faster moving fluid to the measurement plane and decreasing the width of the LMR. There is little to no spanwise movement of the packet, which is also true in other Scenario II runs.

4.2.3. *Scenario III*

Figure 26 illustrates the third scenario in the 0.6δ spacing case. The diverging pattern of black and green swirls just upstream of the upper cylinder suggests that the vortex packet is indeed obstructed and deformed by the cylinder. Similar to the Scenario II examples, the two existing packets are enhanced by the cylinder wakes as the population of streamwise-aligned swirls increases, and also the relative area occupied by $Q2$ Reynolds stresses. Also similar to Scenario II, the $Q2$ events are more focused than the $Q4$ events, as has been documented by Ganapathisubramani *et al.* (2003) and Longmire *et al.* (2011). Both packets migrate gradually towards the mid-spacing location, with the spanwise spacing remaining about 0.6δ throughout the measurement domain. Again, the spanwise movement of the enhanced packets seems to be induced by the downwash behind each cylinder.

Since the 0.4δ cylinder array had a spacing different from the most dominant spanwise scale of 0.6δ in the unperturbed (incoming) flow, a mixed scenario (II and III) was frequently observed for that array, resulting in more disorganization of the downstream flow structures due to the different wake-packet interaction schemes for each scenario. For the 0.6δ array, however, the relative packet-to-cylinder position was

https://doi.org/10.1017/jfm.2014.185 Published online by Cambridge University Press

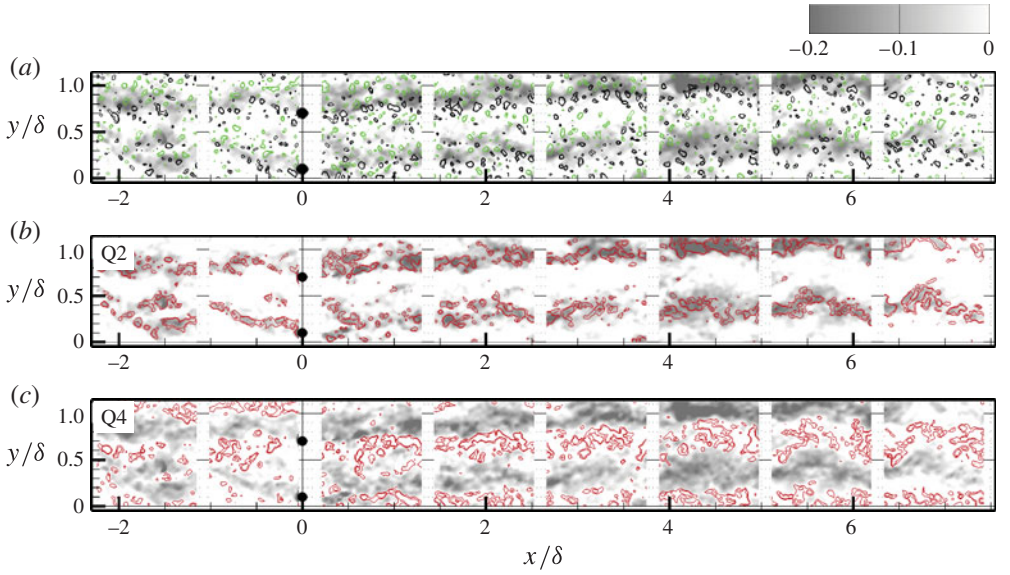


FIGURE 26. (Colour online) Selected run of the 0.6δ spacing case representing scenario III of wake-packet interaction. Consecutive fields are separated by 0.4 s or $1.6\delta/U_\infty$. Grey scale maps the streamwise velocity relative to 0.37 m s^{-1} normalized by $U_\infty =$ 0.508 m s^{-1}. 2D swirling strength is marked by contour lines (black: $\lambda_{ci} > 0.6$, green: $\lambda_{ci} < -0.6$, signed by ω_z). High Reynolds stress ($-uv$) regions of both $Q2$ and $Q4$ events are marked by red contour lines ($Q2 = Q4 = 0.5\sigma_u\sigma_w$).

more likely to be the same for neighbouring packets. Consequently, the wake-packet interactions and development of neighbouring packets were better organized in the downstream flow, helping to explain the greater persistence of the perturbation mode in the 0.6δ case.

5. Conclusions

In the present investigation, PIV experiments were conducted to study the perturbation effects of a single spanwise array of cylinders immersed in the logarithmic region of a turbulent boundary layer. A Fourier transform method was employed to determine the dominant spanwise scales in the flow. Flying PIV was implemented to enable tracking of vortex packet structures in specific runs both upstream and downstream of the cylinder array.

The averaged streamwise velocity fields showed first a splitting of individual cylinder wakes. Neighbouring split wakes then merged into new LMRs at spanwise locations midway between cylinders. The merging location moved further downstream as the cylinder spacing increased. The average wall-normal velocity showed a clear pattern of downwash directly behind each cylinder, which persisted further downstream with increased cylinder spacing. The persistence distance correlated well with the merging locations observed in the averaged streamwise velocity fields, suggesting that downwash played a significant role in the cylinder wake development. Based on measurements extending 7δ downstream of the perturbation, arrays with 0.6δ and 0.8δ yielded the strongest persistence in the spanwise perturbation wavelength. Of these two cases, the 0.6δ array, which matched the most dominant spanwise scale in the unperturbed flow, produced a stronger amplification.

https://doi.org/10.1017/jfm.2014.185 Published online by Cambridge University Press

Features and the evolution of packets or LMRs were observed over streamwise travel distances of 9δ, corresponding to times of $12.4\delta/U_\infty$. In unperturbed flow, approximately 77 % of observed packets remained coherent over this travel distance. The approximate spanwise spacing between the packets matched the dominant spanwise scale of 0.6δ.

The cylinder array with narrowest spacing of 0.2δ generated the strongest perturbation to the flow. In this case, the closely spaced cylinder wakes were very unstable, and strong spanwise interactions between neighboring wakes resulted first in a very disorganized distribution of swirling structures, such that incoming packet signatures at the measurement height largely disappeared. The Fourier transform method revealed a rapid growth in the dominant spanwise scales in the range $0 < x/\delta < 2$ downstream of this array. Interestingly, the downstream flow pattern at a measurement height of $z^+ = 300$ ($z/\delta = 0.12$) recovered rapidly, such that packet signatures observed upstream reappeared at or near their original spanwise locations. This recovery, observed in all FPIV runs with distinct packets in the incoming flow, was quantified by relatively strong cross-correlations between fields upstream and $2–7\delta$ downstream of the perturbation array. This rapid recovery suggests that the upstream packets extended significantly above the perturbation height of $z^+ = 500$ and that their outer layer organization persisted through the perturbation, communicating downwards towards the wall and re-establishing their typical organization as the flow moved downstream. This result might also be interpreted in the following way: the wall-normal and spanwise scales associated with the obstacles in the array are too small to fully disrupt existing packets. This might be comparable to flow over rough walls, where roughness elements with relatively small spanwise spacing and wall-normal extent are distributed over long streamwise distances yet packet structures are also prevalent in the outer region (see e.g. Wu & Christensen 2010).

When the cylinder spacing was increased to 0.4δ or larger, upstream packet signatures persisted through the perturbation array and tended to shift spanwise location at least partially due to the downwash downstream of cylinder tips. The cylinder wake and packet evolution then became more dependent on the upstream packet organization. Based on examination of many runs of the 0.4δ and 0.6δ cases, wake-packet interactions were classified into three scenarios. In the first scenario, where no or only weakly distinct packets were observed in the incoming flow, individual cylinder wakes merged or paired into new LMRs at spanwise locations midway between the cylinders, although roughly 18 % of these new LMRs became indistinct or disappeared by $\sim 6\delta$ downstream. This might result from further spanwise interactions observed in some runs or the out-of-plane movements of the LMRs. In the second scenario, existing packets in the incoming flow passed between neighbouring cylinders, were strengthened by ingesting portions of the nearest wake, and remained coherent in the mid-spacing locations. In the third scenario, incoming packets impinged directly on the cylinders. These packets were enhanced by the coincident cylinder wakes before shifting gradually towards the mid-spacing locations. Consistent with the Fourier data, the FPIV data suggested that the 0.6δ case yielded a more persistent downstream flow organization compared with the 0.4δ case because the spanwise offset between incoming packets and cylinders was more likely to be similar for neighbouring packets.

In all of the perturbed cases, tip downwash effects tended to bring faster moving fluid down to the measurement plane at spanwise locations directly behind each cylinder. In the 0.2δ case, this tip downwash destabilized Kármán-like structures behind the cylinders, yielding strong spanwise interactions between neighbouring

https://doi.org/10.1017/jfm.2014.185 Published online by Cambridge University Press

wakes. For larger array spacings, individual wakes remained independent over longer distances, but the tip downwash nevertheless aided in shifting downstream packet structures towards the mid-span locations.

All of the results in this paper were obtained for a fixed obstacle span D and height H. Considering the effects observed, we would expect that the amount of tip downwash, associated with the lateral shifting of wakes, would scale directly with D, the perturbation span. The previous hot-wire measurements by Ryan *et al.* (2011) showed that thinner cylinders with matched H yielded similar, although weaker perturbation patterns in averaged streamwise velocity statistics at matched x/δ locations. On the other hand, cases with matched D but different H ($H^+ = 100$ versus $H^+ = 150$) yielded similar results up to $z^+ = 100$, suggesting perhaps that although the wall-normal extent of perturbations may be sensitive to changes in obstacle height, the perturbation intensities are relatively insensitive. Thus, it would be interesting to see to what extent the lateral shifting and persistence exhibited downstream of larger array spacings would also occur if H were decreased from the present value.

Although the present results are limited to one measurement height, this height was chosen based on earlier volumetric measurements documenting that averaged perturbations were significant and consistent throughout the logarithmic region. In the future, it would be interesting to examine space/time evolution within volumetric fields to gain a more complete picture of the overall disturbance to incoming packets as well as packet recovery from a 'strong' perturbation as in the 0.2δ spacing case.

Acknowledgements

The authors gratefully acknowledge support from the US National Science Foundation through Grant CBET-0933341. The authors thank Dr Cecilia Ortiz-Dueñas and Mitchell Ryan for assistance with the experiments and insights on the results.

REFERENCES

ADRIAN, R. J. 2007 Hairpin vortex organization in wall turbulence. *Phys. Fluids* **19** (4), 041301.

ADRIAN, R. J. & LIU, Z. C. 2002 Observation of vortex packets in direct numerical simulation of fully turbulent channel flow. *J. Visual.-Japan* **5** (1), 9–19.

ADRIAN, R. J., MEINHART, C. D. & TOMKINS, C. D. 2000 Vortex organization in the outer region of the turbulent boundary layer. *J. Fluid Mech.* **422**, 1–54.

ATKINSON, C., CHUMAKOV, S., BERMEJO-MORENO, I. & SORIA, J. 2012 Lagrangian evolution of the invariants of the velocity gradient tensor in a turbulent boundary layer. *Phys. Fluids* **24** (10), 1–14.

BELCHER, S. E., JERRAM, N. & HUNT, J. C. R. 2003 Adjustment of a turbulent boundary layer to a canopy of roughness elements. *J. Fluid Mech.* **488**, 369–398.

CASTRO, I. P., CHENG, H. & REYNOLDS, R. 2006 Turbulence over urban-type roughness: deductions from wind-tunnel measurements. *Boundary-Layer Meteorol.* **118** (1), 109–131.

CHRISTENSEN, K. T. & ADRIAN, R. J. 2001 Statistical evidence of hairpin vortex packets in wall turbulence. *J. Fluid Mech.* **431**, 433–443.

COCEAL, O., DOBRE, A., THOMAS, T. G. & BELCHER, S. E. 2007 Structure of turbulent flow over regular arrays of cubical roughness. *J. Fluid Mech.* **589**, 375–409.

DENNIS, D. J. C. & NICKELS, T. B. 2011*a* Experimental measurement of large-scale three-dimensional structures in a turbulent boundary layer. Part 1. Vortex packets. *J. Fluid Mech.* **673**, 180–217.

DENNIS, D. J. C. & NICKELS, T. B. 2011*b* Experimental measurement of large-scale three-dimensional structures in a turbulent boundary layer. Part 2. Long structures. *J. Fluid Mech.* **673**, 218–244.

https://doi.org/10.1017/jfm.2014.185 Published online by Cambridge University Press

DILLON-GIBBONS, C. J., WONG, C. Y., CHEN, L. & SORIA, J. 2007 Cylinder wake - boundary layer interaction in the near field. In *Proceedings of 16th Australasian Fluid Mechanics Conference, Gold Coast, Australia* (ed. P. Jacobs, P. McIntyre, M. Cleary, D. Buttsworth, D. Mee, C. Rose, R. Morgan & C. Lemckert), pp. 1475–1480. School of Engineering, The University of Queensland.

ELSINGA, G. E., ADRIAN, R. J., VAN OUDHEUSDEN, B. W. & SCARANO, F. 2010 Three-dimensional vortex organization in a high-Reynolds-number supersonic turbulent boundary layer. *J. Fluid Mech.* **644**, 35–60.

ELSINGA, G. E., KUIK, D. J., VAN OUDHEUSDEN, B. W. & SCARANO, F. 2007 Investigation of the three-dimensional coherent structures in a turbulent boundary layer with tomographic-PIV. In *Proceedings of 45th AIAA Aerospace Sciences Meeting and Exhibit, Reno, NV, USA*, AIAA.

ELSINGA, G. E. & MARUSIC, I. 2010 Evolution and lifetimes of flow topology in a turbulent boundary layer. *Phys. Fluids* **22** (1), 1–9.

ELSINGA, G. E., POELMA, C., SCHRÖDER, A., GEISLER, R., SCARANO, F. & WESTERWEEL, J. 2012 Tracking of vortices in a turbulent boundary layer. *J. Fluid Mech.* **697**, 273–295.

GANAPATHISUBRAMANI, B., HUTCHINS, N., HAMBLETON, W. T., LONGMIRE, E. K. & MARUSIC, I. 2005 Investigation of large-scale coherence in a turbulent boundary layer using two-point correlations. *J. Fluid Mech.* **524**, 57–80.

GANAPATHISUBRAMANI, B., LONGMIRE, E. K. & MARUSIC, I. 2003 Characteristics of vortex packets in turbulent boundary layers. *J. Fluid Mech.* **478**, 35–46.

GANAPATHISUBRAMANI, B., LONGMIRE, E. K. & MARUSIC, I. 2006 Experimental investigation of vortex properties in a turbulent boundary layer. *Phys. Fluids* **18** (5), 1–14.

GAO, Q. 2011 Evolution of eddies and packets in turbulent boundary layers. PhD thesis, University of Minnesota Twin Cities.

GAO, Q., ORTIZ-DUEÑAS, C. & LONGMIRE, E. K. 2013 Evolution of coherent structures in turbulent boundary layers based on moving tomographic PIV. *Exp. Fluids* **54** (12), 1–16.

GUALA, M., TOMKINS, C. D., CHRISTENSEN, K. T. & ADRIAN, R. J. 2012 Vortex organization in a turbulent boundary layer overlying sparse roughness elements. *J. Hydraul Res.* **50** (5), 465–481.

HAIN, R., KÄHLER, C. J. & MICHAELIS, D. 2008 Tomographic and time resolved PIV measurements on a finite cylinder mounted on a flat plate. *Exp. Fluids* **45**, 715–724.

HUTCHINS, N., GANAPATHISUBRAMANI, B. & MARUSIC, I. 2005b Spanwise periodicity and the existence of very large scale coherence in turbulent boundary layers. In *Proceedings of Turbulence and Shear Flow Phenomena IV, Williamsburg, VA, USA*. TSFP.

HUTCHINS, N., HAMBLETON, W. T. & MARUSIC, I. 2005*a* Inclined cross-stream stereo particle image velocimetry measurements in turbulent boundary layers. *J. Fluid Mech.* **541**, 21–54.

HUTCHINS, N. & MARUSIC, I. 2007 Evidence of very long meandering features in the logarithmic region of turbulent boundary layers. *J. Fluid Mech.* **579**, 1–28.

IKEDA, T. & DURBIN, P. A. 2007 Direct simulations of a rough-wall channel flow. *J. Fluid Mech.* **571**, 235–263.

JACOBI, I. & MCKEON, B. J. 2011 New perspectives on the impulsive roughness-perturbation of a turbulent boundary layer. *J. Fluid Mech.* **677**, 179–203.

JIMÉNEZ, J. 2004 Turbulent flows over rough walls. *Annu. Rev. Fluid Mech.* **36** (1), 173–196.

LEE, J. H. & SUNG, H. J. 2011 Very-large-scale motions in a turbulent boundary layer. *J. Fluid Mech.* **673**, 80–120.

LEHEW, J. A., GUALA, M. & MCKEON, B. J. 2013 Time-resolved measurements of coherent structures in the turbulent boundary layer. *Exp. Fluids* **54** (4), 1–16.

LONGMIRE, E. K., GAO, Q., RYAN, M. D. & ORTIZ-DUEÑAS, C. 2011 Examination of turbulent boundary layers by volumetric velocimetry. In *Proceedings of 9th International Symposium on Particle Image Velocimetry, Kobe, Japan*. International Symposium on Particle Image Velocimetry.

MATHIS, R., HUTCHINS, N. & MARUSIC, I. 2009 Large-scale amplitude modulation of the small-scale structures in turbulent boundary layers. *J. Fluid Mech.* **628**, 311–337.

https://doi.org/10.1017/jfm.2014.185 Published online by Cambridge University Press

ORLANDI, P., LEONARDI, S. & ANTONIA, R. A. 2006 Turbulent channel flow with either transverse or longitudinal roughness elements on one wall. *J. Fluid Mech.* **561**, 279–305.

ORTIZ-DUEÑAS, C., RYAN, M. D. & LONGMIRE, E. K. 2011 Modification of turbulent boundary layer structure using immersed wall-mounted cylinders. In *Proceedings of Turbulence and Shear Flow Phenomena VII, Ottawa, Canada*. TSFP.

PARK, C. W. & LEE, S. J. 2002 Flow structure around a finite circular cylinder embedded in various atmospheric boundary layers. *Fluid Dyn. Res.* **30** (4), 197–215.

PARK, C. W. & LEE, S. J. 2003 Flow structure around two finite circular cylinders located in an atmospheric boundary layer: side-by-side arrangement. *J. Fluids Struct.* **17** (8), 1043–1058.

PUJALS, G., COSSU, C. & DEPARDON, S. 2010 Forcing large-scale coherent streaks in a zero-pressure-gradient turbulent boundary layer. *J. Turbul.* **11** (25), 1–13.

RYAN, M. D. 2011 Planar and volumetric measurements downstream of cylinders immersed in a turbulent boundary layer. Master's thesis, University of Minnesota Twin Cities.

RYAN, M. D., ORTIZ-DUEÑAS, C. & LONGMIRE, E. K. 2011 Effects of simple wall-mounted cylinder arrangements on a turbulent boundary layer. *AIAA J.* **49** (10), 2210–2220.

SAKAMOTO, H. & ARIE, M. 1983 Vortex shedding from a rectangular prism and a circular-cylinder placed vertically in a turbulent boundary-layer. *J. Fluid Mech.* **126**, 147–165.

SCHOFIELD, W. H. & LOGAN, E. 1988 Viscous flow around two and three-dimensional wall mounted obstacles. In *Proceedings of 1st AIAA, ASME, SIAM, and APS, National Fluid Dynamics Congress, Cincinnati, OH, USA*, pp. 1742–1748. AIAA.

SIMPSON, R. L. 2001 Junction flows. *Annu. Rev. Fluid Mech.* **33**, 415–443.

SUMNER, D., HESELTINE, J. L. & DANSEREAU, O. J. P. 2004 Wake structure of a finite circular cylinder of small aspect ratio. *Exp. Fluids* **37** (5), 720–730.

TOMKINS, C. D. 2001 The structure of turbulence over smooth and rough walls. PhD thesis, University of Illinois at Urbana–Champaign.

TOMKINS, C. D. & ADRIAN, R. J. 2003 Spanwise structure and scale growth in turbulent boundary layers. *J. Fluid Mech.* **490**, 37–74.

WANG, H. F., ZHOU, Y., CHAN, C. & LAM, K. 2006 Effect of initial conditions on interaction between a boundary layer and a wall-mounted finite-length-cylinder wake. *Phys. Fluids* **18** (6), 1–12.

WARK, C. E., NAGUIB, A. M. & NAGIB, H. M. 1990 Effect of plate manipulators on coherent structures in a turbulent boundary-layer. *AIAA J.* **28** (11), 1877–1884.

WARK, C. E., NAGUIB, A. M. & ROBINSON, S. K. 1991 Scaling of spanwise length scales in a turbulent boundary layer. In *Proceedings of 29th AIAA Aerospace Sciences Meeting, Reno, NV, USA*. AIAA.

WESTERWEEL, J. 1994 Efficient detection of spurious vectors in particle image velocimetry data. *Exp. Fluids* **16**, 236–247.

WESTERWEEL, J., DABIRI, D. & GHARIB, M. 1997 The effect of a discrete window offset on the accuracy of cross-correlation analysis of digital PIV recordings. *Exp. Fluids* **23** (1), 20–28.

WIENEKE, B. 2005 Stereo-PIV using self-calibration on particle images. *Exp. Fluids* **39**, 267–280.

WILLIAMSON, C. H. K. 1996 Vortex dynamics in the cylinder wake. *Annu. Rev. Fluid Mech.* **28** (1), 477–539.

WU, Y. & CHRISTENSEN, K. T. 2010 Spatial structure of a turbulent boundary layer with irregular surface roughness. *J. Fluid Mech.* **655**, 380–418.

ZHENG, S. 2013 Perturbing spanwise modes in turbulent boundary layers. Master's thesis, University of Minnesota Twin Cities.

ZHOU, J., ADRIAN, R. J., BALACHANDAR, S. & KENDALL, T. M. 1999 Mechanisms for generating coherent packets of hairpin vortices in channel flow. *J. Fluid Mech.* **387**, 353–396.

https://doi.org/10.1017/jfm.2014.185 Published online by Cambridge University Press